PCCP

ARTICLE TYPE

Cite this: DOI: 00.0000/xxxxxxxxxx

Grazing incidence fast atom and molecule diffraction: Theoretical challenges

Cristina Díaz[a], María Silvia Gravielle[b]

Received Date
Accepted Date

DOI: 00.0000/xxxxxxxxxx

This perspective article reviews the state-of-the-art of grazing incidence fast atom and molecule diffraction (GIFAD and GIFMD) simulations and addresses the main challenges that theorists, aiming to provide useful inputs in this topic, are facing. We first discuss briefly the methods used to build accurate potential energy surfaces describing the interaction between the projectile and the surface. Subsequently, we focus on the dynamics simulation methods for GIFAD, a phenomenon that has received a lot of experimental attention since 2007, when first measurements were published. Following this experimental effort theorists have developed and adapted a bunch of methods able to simulate, analyzed and extract information from the experimental outputs. We review these methods, from the very simple ones based on classical dynamics to the full quantum ones, paying special attention to the more versatile semiclassical approaches, which include quantum ingredients in the dynamics at a computational cost only slightly higher than that required in classical dynamics. Within the semiclassical framework it is possible, for example, to include in the dynamics the surface phonons and the projectile coherence, two factors that may have a relevant influence on the experimental measurements, at a reasonable computational cost. Finally, we address GIFMD, a phenomenon that have received much less attention and for which there is still a lot of room for research. We review the few examples of GIFMD available in the literature, and we discuss new phenomena associated with the molecular internal degrees of freedom, which may have some impact in other close relative fields, such as molecular reactivity on metal surfaces. Finally, we point out opened questions, raised from the comparisons between theoretical and experimental results, which claim for further experimental efforts.

1 Introduction

The first measurements[1,2], in 2007, of atomic diffraction spectra upon scattering under fast (200 eV - 2 keV) grazing (0.2°-2°) incidence opened the doors to the development of a new accurate analysis technique in surface science, as both an alternative and a complementary tool to thermal-energy atom and molecule scattering (TEAS and TEMS)[3–7]. Grazing incidence fast atom and molecule diffraction (GIFAD and GIFMD) allows, on the one hand, to reach areas of the potential energy surfaces (PESs) unreachable to TEAS and TEMS, and, on the other hand, to minimize the influence of surface vibrations (phonons) on the measurements, whilst electronic excitations do not represent a major problem than in TEAS or TEMS.

The physical mechanism behind this phenomenon is the strong decoupling between the fast motion parallel to the surface and the slow motion perpendicular to it[8]. Due to the fast grazing incidence conditions (see Fig. 1 (a)), we can assume that the initial momentum of the projectile is much larger than the momentum change in the collision, responsible for the observed diffraction peaks, and therefore, to zero order perturbation theory, the velocity of the projectile along the incidence direction, v_x, can be considered as constant, so that the projectile feels a periodic potential (V) in that direction. If we call a_x the one-dimensional lattice parameter (the potential periodicity parameter) along the incidence direction ($\hat{\mathbf{x}}$), it is possible to compute the longitudinal and transverse momentum change over a_x, to first order perturbation theory, as:

$$\Delta K_x^{||} = -\frac{1}{v_x}\int_0^{a_x} dx \frac{\partial V}{\partial x} = \frac{1}{v_x}[-V(a_x,y)+V(0,y)] = 0,$$
$$\Delta K_y^{||} = -\frac{1}{v_x}\int_0^{a_x} dx \frac{\partial V}{\partial y} \neq 0. \quad (1)$$

From these equations one can see that the momentum change along the incidence direction is of second order, which means that any acceleration is compensated by a slowing down. Whereas the momentum change along the transverse direction ($\hat{\mathbf{y}}$) is of first

[a]Departamento de Química Física, Facultad de CC. Químicas, Universidad Complutense de Madrid, 28040 Madrid, Spain; E-mail: crdiaz08@ucm.es
[b]Instituto de Astronomía y Física del Espacio (IAFE, UBA-CONICET), Ciudad Universitaria, C1428EGA, Buenos Aires, Argentina; E-mail: msilvia@iafe.uba.ar

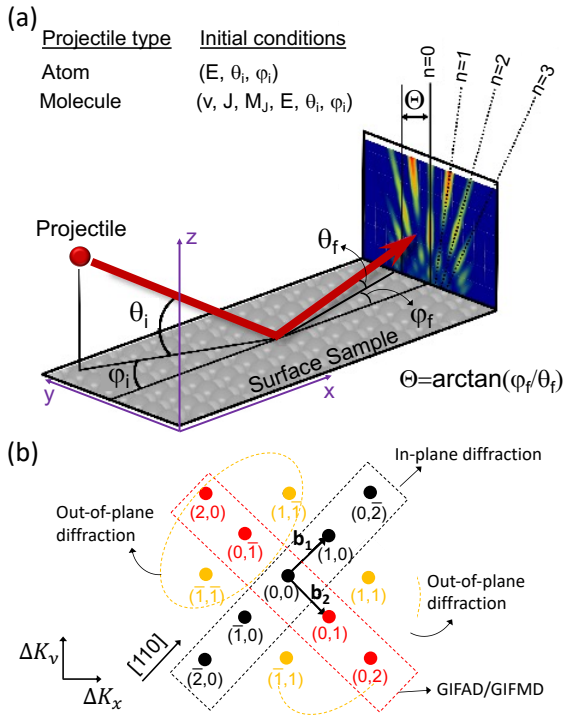

Fig. 1 (Color online) (a) Schematic representation of a grazing incidence diffraction process. In the detection plane both the deflection angle Θ and the diffraction order n are indicated. (b) In-plane (black dots) and out-of-plane (orange and red dots) diffraction definition for incidence along the [110] crystallographic direction. Red dots indicate the diffraction peaks observed in GIFAD and GIFMD.

order, which means that the effect of the transverse force is cumulative. Thus, by far the main momentum transfer in the projectile is from the slow motion perpendicular to the surface (K_z) to K_y. In typical GIFAD experiments, the projectile de Broglie wavelength (λ) is much smaller than the shortest interatomic distances in the crystal (the lattice constant for single-atom crystals), making unexpected the observation of quantum interference. But as the wavelength $\lambda_\perp$ associated with the perpendicular motion is of the order of magnitude of the surface lattice constant, according to the Bragg's law it is possible to observe diffraction whenever ΔK_y coincides with a reciprocal lattice vector. Furthermore, as $\Delta K_x \simeq 0$ only out-of-plane diffraction peaks, perpendicular to the incidence direction,are observed (see Fig. 1 (b) for the definition of in-plane and out-of-plane diffraction). Strictly speaking, the requirement of a periodic potential is only fulfilled for trajectories parallel to the surface because whenever the incidence angle is $\theta_i > 0^\circ$ the potential depends on the z coordinate, normal to the surface plane. However, if the potential barely varies over the interval $\delta z = a_x \tan\theta_i$ the potential can be considered as periodic, and this is the case if $(\partial V/\partial z)\delta z << E$, i.e., if $a_x << E\ [\tan\theta_i(\partial V/\partial z)]^{-1}$. This condition is better fulfilled for incidence along symmetry directions with low Miller indices. Hence, GIFAD patterns are essentially governed by the normal incidence energy $E_\perp = E sin^2\theta_i$, associated with the motion in the plane perpendicular to the axial direction[2,9,10].

Since those first measurements[1,2], GIFMD and, more intensively, GIFAD have been widely used as a surface analysis tool (see Refs.[11,12] and references therein). First experiments were carried out for isolating surfaces, LiF(001)[1,2,9,13–15] and NaCl(001)[2,16,17], using atomic projectiles, He, H and D. Later on, GIFAD was also used to analyze semiconductors, such as Ga_2O_3(100)[18], ZnSe(001) epilayer grown on a GaAs(001) substrate[19], a $\beta_2(2\times4)$ reconstructed GaAs(001) surface[20,21], and a (12×4) reconstructed Al_2O_3 $(11\bar{2}0)$ surface[22,23]. GIFAD has also been shown to work for metal surfaces[24,25], despite electronic excitations. More complex surfaces, such as Fe(001)[26,27] and Mo(112)[28] covered with atomic (O and S) superstructures, and even monolayers adsorbed on insulating and metal surfaces, have been analyzed by means of GIFAD. Examples of this latter case are graphene grown on 6H-SiC(0001)[29] and silica adsorbed on Mo(112)[30,31]. The GIFAD technique has been even applied to study organic molecules adsorbed on metals, for example, alanine amino acid adsorbed on Cu(110)[32,33]. Furthermore, it is worth pointing out that GIFAD can be used to follow dynamics processes in real time, such as the grow of GaAs[34] and the crystallization of perylene on Ag(110)[35].

This intense experimental effort has triggered the development and improvement of theoretical tools able to account for, and to support, experimental measurements. Here, we review these theoretical methods, all of them based on the validity of the Bohr-Oppenheimer approximation, focusing on their successes and shortcomings, as well as the challenges they have to face. Since insulating crystals were widely study via GIFAD, most of the examples presented throughout the article to illustrate the performance of the different theoretical approaches will refer to this type of material. However, the application of these methods to other surfaces, like semiconductors or metals, is straightforward. Atomic units (a.u.) are used unless otherwise stated.

2 Electronic structure description

The exceptional sensitivity of the diffraction patterns to the morphological and electronic features of the crystal surface is one of the most valuable qualities of GIFAD, which makes it a powerful technique for surface analysis. From the theoretical point of view, it is precisely this property which transforms the projectile-surface potential in a key ingredient, whose proper description represents a real challenge. Even the more elaborated potential models, like those based on accurate density functional theory (DFT) calculations, which are adequate for atom-surface scattering at thermal energies, may fail to describe GIFAD patterns, sometimes requiring the incorporation of *ad hoc* parameters to obtain a quantitative agreement with the experimental data[20].

In this Section, we will analyze two different kinds of projectile-surface potential models, which are usually employed in GIFAD descriptions.

2.1 Analytical potentials

In relation to the crystal target, although the GIFAD method was applied to a wide variety of materials, the LiF(001) surface used in the first experiments[1,2] is still considered as an ideal benchmark to investigate different GIFAD mechanisms[15,37–40]. Then,

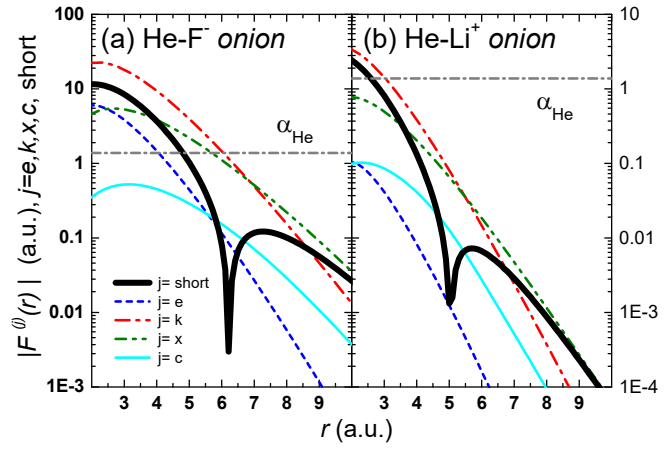

Fig. 2 (Color online) Partial *short-range* contributions to the binary He-*onion* potential. Absolute value of $F^{(j)}_{\mathbf{r}_B}(r)$, $j = e, k, x, c$, short (as defined in the text) as a function of the internuclear distance r, for the interaction with (a) a F^- and (b) a Li^+ *onions*. For comparison, the horizontal dashed line indicates the value of the atomic helium polarizability α_{He}. Reproduced from Ref.[36] with permission from World Scientific, copyright 2019

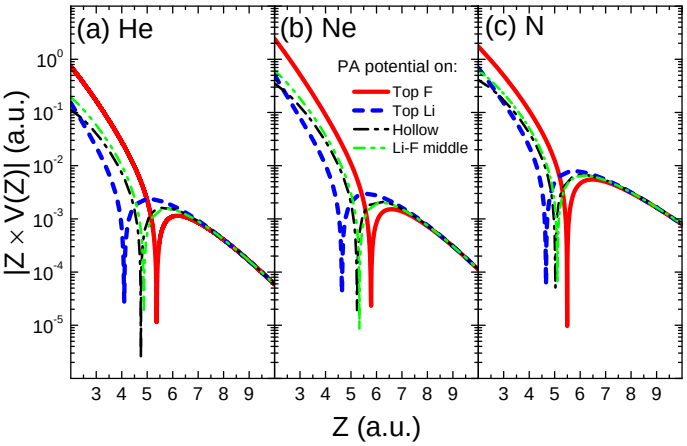

Fig. 3 (Color online) Absolute value of the PA atom-surface potential $V(Z)$, given by Eq. (2), for He, Ne (closed-shell) and N (open-shell) projectiles, as a function of the normal atom-surface distance Z. Different high-symmetry positions on the LiF(001) surface are considered. Data taken from Ref.[36].

it will be here used to show the performance of analytical potentials derived from pairwise additive (PA) models[36,41]. Note that for insulating materials, like LiF, the electron density is highly localized around the atomic nuclei, supporting the use of PA potential models as a reliable alternative to more correct, in principle, self-consistent descriptions. Within the framework of GIFAD, PA potentials were also successfully used to describe more complex surfaces, like superstructures of O and S atoms on a Fe(110) surface[26] or a $\beta - Ga_2O_3(100)$ surface[18]. But in the case of metals, the localized electron-density condition is not met, making inevitable the use of self-consistent potentials, such as those obtained from DFT calculations.

PA potentials are built as a sum of binary interatomic potentials that represent the interaction of the atomic projectile with individual atomic centers in the crystal. Despite these potentials are simpler than those obtained from DFT calculations (see Sec, 2.2), they have shown to provide an adequate representation of the atom-surface interaction for insulator materials[42–44], becoming a useful tool to analyze its different contributions (see also Sec. 4.2), as well as to incorporate crystal defects[45] or lattice vibrations[38] in GIFAD with a lower computational cost. Recently, they were also applied as a starting point to derive an empirical Ne/LiF(001) potential from experimental GIFAD patterns[15].

In particular, PA potentials for neutral atoms placed in front of a LiF(001) surface have been extensively studied over the years[46–49] due to their relevance in different fields. However, these analytical models were recently improved by incorporating non-local contributions of the electron density, along with a more realistic description of the electron density associated with each ionic center of the insulator[41]. Within this renewed PA model[36,41], the atom-surface interaction $V(\mathbf{R})$ is split into *short-* and *long- range* contributions as:

$$V(\mathbf{R}) = \sum_{\mathbf{r}_B} c_{\mathbf{r}_B} v^{(\text{short})}_{\mathbf{r}_B}(\mathbf{R} - \mathbf{r}_B) + W^{(\text{long})}(\mathbf{R}), \qquad (2)$$

where $\mathbf{R}$ denotes the position vector of the incident atom, $v^{(\text{short})}_{\mathbf{r}_B}(\mathbf{r})$ describes the *short-range* binary interaction between the atomic projectile and the crystal ion placed at the Bravais lattice site $\mathbf{r}_B$, as a function of the relative vector $\mathbf{r}$, and the sum over $\mathbf{r}_B$ covers all occupied sites of the crystal sample, taking into account the surface rumpling[9] (i.e., the outward (inward) shift of the positions of the topmost F^- (Li^+) ions with respect to the unreconstructed surface). In Eq. (2), the factors $c_{\mathbf{r}_B}$ are given by the Evjen caging[50], while the potential $W^{(\text{long})}(\mathbf{R})$ describes the *long-range* projectile-surface interaction due to the effect of dispersive forces.

The binary potentials $v^{(\text{short})}_{\mathbf{r}_B}$ depend on the unperturbed electron densities of the interacting partners, which are considered as frozen. But in this upgraded version of the PA model, the electron density of the crystal ion at $\mathbf{r}_B$ is affected by the ionic charges around it as given by the *onion* approximation[51]. This approach considers the effect of the ionic lattice as spherical charged shells around the $\mathbf{r}_B$ site, giving rise to an *onion* density $n^{(O)}_{\mathbf{r}_B}(r')$ for F^- and Li^+ sites (r' being the distance to the lattice site $\mathbf{r}_B$), which is derived from Hartree-Fock wave functions that include the contribution of this spherical Madelung potential[41].

Using the radial-dependent atom and *onion* densities, $v_{\mathbf{r}_B}^{(\mathrm{short})}$ is obtained as the sum of the electrostatic (e), kinetic (k), exchange (x) and correlation (c) contributions:

$$v_{\mathbf{r}_B}^{(\mathrm{short})}(\mathbf{r}) = e_{\mathbf{r}_B}^{(\mathrm{e})}(\mathbf{r}) + e_{\mathbf{r}_B}^{(\mathrm{k})}(\mathbf{r}) + e_{\mathbf{r}_B}^{(\mathrm{x})}(\mathbf{r}) + e_{\mathbf{r}_B}^{(\mathrm{c})}(\mathbf{r}), \tag{3}$$

where $e_{\mathbf{r}_B}^{(\mathrm{e})}(\mathbf{r})$ corresponds to the Coulomb interaction between the atomic projectile and the *onion* placed at $\mathbf{r}_B$. The other terms of Eq. (3) are derived from well-established non-local functionals: $e_{\mathbf{r}_B}^{(\mathrm{k})}(\mathbf{r})$ is evaluated with the Lee-Lee-Parr approach[52], $e_{\mathbf{r}_B}^{(\mathrm{x})}(\mathbf{r})$ with the spin-dependent Becke approximation[53], and $e_{\mathbf{r}_B}^{(\mathrm{c})}(\mathbf{r})$ with the Lee-Yang-Parr functional[54]. All these functionals include the gradient and/or Laplacian of the involved electron densities, accounting for the non-uniform behavior of the electron distributions.

As an example, in Fig. 2, we show the different terms of $v_{\mathbf{r}_B}^{(\mathrm{short})}$ for He projectiles interacting with F^- and Li^+ *onions*[36,41]. These partial potentials are displayed by means of the function $F_{\mathbf{r}_B}^{(\mathrm{j})}(r) = r(1+2r^3)e_{\mathbf{r}_B}^{(\mathrm{j})}(r)$, with j = e, k, x, c, in order to analyze their asymptotic limits. Since the absolute values of $F_{\mathbf{r}_B}^{(\mathrm{j})}(r)$ are plotted in Fig. 2, the signs must be indicate: $F_{\mathbf{r}_B}^{(\mathrm{k})}(r) > 0$, $F_{\mathbf{r}_B}^{(\mathrm{x})}(r) < 0$, $F_{\mathbf{r}_B}^{(\mathrm{c})}(r) < 0$, and $F_{\mathbf{r}_B}^{(\mathrm{e})}(r) > 0$, except for the interaction with the F^- *onion*, whose electrostatic potential becomes negative for $r \gtrsim 1$ a.u.. For both F^- and Li^+ *onions*, $F_{\mathbf{r}_B}^{(\mathrm{short})}(r) = r(1+2r^3)v_{\mathbf{r}_B}^{(\mathrm{short})}(r)$ is positive at small distances, being dominated by the electrostatic contribution. In fact, as a consequence of the predominance of the internuclear repulsion, $F_{\mathbf{r}_B}^{(\mathrm{short})}(r) \to F_{\mathbf{r}_B}^{(\mathrm{e})}(0) = Z_A Z_O$ as $r \to 0$, with Z_A (Z_O) being the atom (*onion*) nuclear charge. But when r increases, the kinetic, exchange and correlation terms become sequentially relevant, causing the change of sign of $F_{\mathbf{r}_B}^{(\mathrm{short})}$, as indicated by the dip of the curve in both panels of Fig. 2. Hence, $v_{\mathbf{r}_B}^{(\mathrm{short})}$ is repulsive at short distances but becomes attractive as r increases, presenting an attractive well, feature that is reflected in the total PA potential (see Fig. 3).

In contrast with the *short-range* potential, the *long-range*[41] contribution takes into account the rearrangement of the atom and *onion* electron densities as a result of their mutual interaction. Far from the surface, where $W^{(\mathrm{long})}(\mathbf{R})$ prevails, the *long-range* binary potentials $v_{\mathbf{r}_B}^{(\mathrm{long})}(\mathbf{r})$ can be expanded as $v_{\mathbf{r}_B}^{(\mathrm{long})}(\mathbf{r}) \simeq -\alpha_p/(2r^4) - C_{\mathrm{vdW}}/r^6 - \ldots$, where α_p denotes the static polarizability of the atomic projectile, while the parameter C_{vdW} is related to van der Waals (vdW) forces[41]. From Fig. 2, it is clear that the projectile polarization term dominates the PA potential as r increases, leading to

$$W^{(\mathrm{long})}(\mathbf{R}) \simeq -\frac{\alpha_p}{2}\left|\sum_{\mathbf{r}_B}\mathbf{E}_{\mathbf{r}_B}(\mathbf{R}-\mathbf{r}_B)\right|^2, \tag{4}$$

where $\mathbf{E}_{\mathbf{r}_B}(\mathbf{r})$ is the electric field originated by the asymptotic charge $Z_{\mathbf{r}_B}^{(\mathrm{asym})}$ of the *onion* placed at $\mathbf{r}_B$ (with $Z_{\mathbf{r}_B}^{(\mathrm{asym})} = -1, +1$ for F^- and Li^+ *onions*, respectively).

Lastly, Fig. 3 shows the total PA potential for selected closed- and open- shell atoms interacting with a LiF(001) surface at different positions on top of high-symmetry sites. These potentials will be tested by means of GIFAD in Sec. 3.2. Notice that in all the cases, the absolute value of $V(\mathbf{R})$ presents a sharp dip, corresponding to the edge of the attractive well where the PA potential changes its sign. Remarkably, this shallow attractive well, which plays an important role in GIFAD[15,55], is observed even without considering the contribution of vdW dispersive forces, which are usually assumed as responsible for the attractive well[20]. In this regard, note that not only the projectile polarization term (Eq. (4)) does contribute to the well formation but also the exchange and correlation terms of Eq. (3).

2.2 DFT-based potentials

Generally speaking, to develop a DFT-based potential energy surface one has to computed a set of DFT energies, which is subsequently interpolated (see Sec. 2.2.1) to obtain a continuous representation of the potential energy surface (PES). Thanks to the flexibility of these interpolations methods, this type of potentials are, in principle, more accurate than the analytical ones, specially when metal surfaces are involved[56]. Although they are subject to the shortcomings of DFT as discussed throughout this section.

In computing the DFT energy for a given system, one has to considered several assumptions and parameters, among them:

- Periodicity of the system. The systems we are dealing with are semiperiodic, that is, only periodic on the surface plane. However, the most popular DFT codes[57–62] apply periodic boundary conditions (PBC) in the three dimensions of space. To solve this problem, a supercell is defined (number of surface layers and dimensions) in such a way that results do not depend on the chosen model, and that the projectile does not interact either with its periodic images or with the top periodic surface.

- Representation of the Brillouin zone (BZ). The number of k points needed to represent the BZ depends on the size of the supercell, so that, for large BZ only the Γ-point is required. Several schemes have been proposed to represent the BZ, the Monkhorst-Pack[63] and the Chadi-Cohen[64] being the most popular.

- Description of the core electrons. To speed up the computational time, most DFT codes consider only the valence electrons in the calculations, whereas the core electrons are treated approximately. Also in this case, several schemes have been proposed, such as the use of norm-conserving[65] and nonlocal ultrasoft[66] pseudopotentials and the projector augmented wave (PAW) method[67].

- Description of the electronic exchange-correlation energy. As the exact form of the exchange-correlation (XC) density functional is unknown, a great deal of effort has gone into developing approximate, but accurate, XC functionals. This effort has given rise to a considerable amount of different functionals (see, for instance,[68,69], and Refs. therein) from the non-empirical functionals, developed ensuring that they meet known exact limits, such as the simple local density approximation (LDA)[70] and those framed within the generalized gradient approximation (GGA)[71], PBE being the

most popular[72] in PBC calculations, to the semi-empirical functionals developed by fitting experimental or theoretical data[73]. However, all these functionals suffer from a common shortcoming, namely the lack of a proper description of long-range dispersion forces. In Sec. 2.3, we discuss in detail this issue in the context of GIFAD and GIFMD.

2.2.1 Interpolation methods

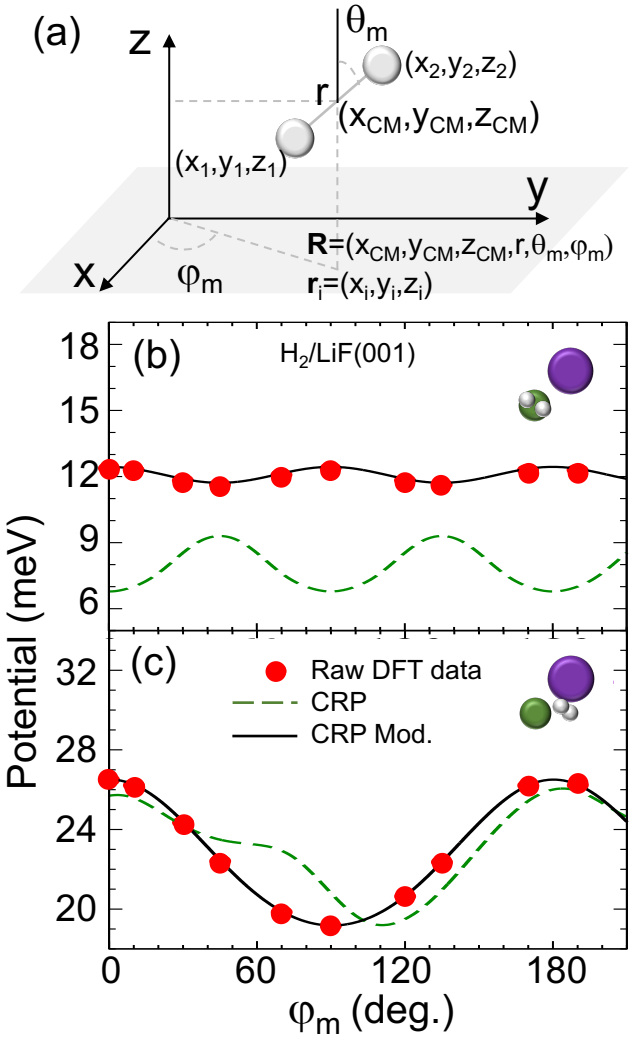

Fig. 4 (Color online) Top panel: (a) Depiction of the coordinate system. Bottom panels: Raw DFT data and interpolated 1D potentials with the standard and modified CRP methods, along the azimuthal angle (φ_m). (b) $Z = 2.96$ Å, $\theta_m = 90°$, and a high symmetry site; (c) $Z = 2.46$ Å, $\theta_m = 30°$, and a low symmetry site. In all the panels the interatomic distance r is kept equal to 0.80 Å. Reprinted with permission from (A. S. Muzas, M. del Cueto, F. Gatti, M. F. Somers, G. J. Kroes, F. Martín, C. Díaz, Phys. Rev. B, H_2/LiF(001) diffractive scattering under fast grazing incidence using a DFT-based potential energy surface, **96**, 205432, 2017). Copyright (2017) by the American Physical Society.

Several interpolation methods able to provide accurate PESs are nowadays available, such as reactive force fields (RFF)[74], neural networks (NN)[75,76], permutation invariant polynomial neural networks (PIP-NN)[77], the modified Shepard interpolation method (MSI)[78,79], and the corrugation reducing procedure (CRP)[80]. From these methods, the latter is by far the most used in the context of GIFAD[55,81–85] and GIFMD[86].

In the original version of the CRP method[80] the PES is decomposed in two terms, a smooth function and a highly corrugated term. So that, within the frozen surface approximation, for diatomic molecular projectiles the six-dimensional (6D) PES (see Fig. 4 (a) for coordinate definitions) can be written as:

$$V_{6D}(\mathbf{R}) = I_{6D}(\mathbf{R}) + V_{3D}(\mathbf{r_1}) + V_{3D}(\mathbf{r_2}), \tag{5}$$

where I_{6D} represent the 6D smooth function that can be easily interpolated following in order the subsequent steps:

- A cubic spline interpolation is performed over (Z_{CM}, r).
- A Fourier interpolation is performed over (X_{CM}, Y_{CM}).
- A Fourier interpolation over (θ_m, φ_m) is performed for each high symmetry site.

In Eq. (5), $V_{3D}(\mathbf{r})$ represents the interaction between one atom of the molecule and the surface, i.e., the highly corrugated term.

Similarly, for atomic projectiles the three-dimensional (3D) PES can be written as:

$$V_{3D}(\mathbf{r}) = I_{3D}(\mathbf{r}) + \sum_{j=1}^{m_a} \sum_{i=1}^{n_a} V_{1D}^{j}(\mathbf{r_i}), \tag{6}$$

where I_{3D} represents the 3D smooth function, which can be easily interpolated using cubic spline functions, and $V_{1D}(\mathbf{r})$ represents the interaction between the projectile and one atom of the surface. In the summations, m_a represents the number of different types of atoms and n_a the number of neighbor surface atoms considered in the interaction.

For molecule(atom)-metal surface interactions, this method has been widely proven to yield very accurate results (see Ref.[87] for a few examples). However, for insulating surfaces a direct application of the general CRP formulation leads to inaccuracies in the interpolation, as shown in Figs. 4 (b) and 4 (c) for the case of H_2/LiF(001). This problem can be solved by introducing a switch function ($L_{Z_0 \delta Z}(\mathbf{r})$) in order to control the CRP applied, so that:

$$V_{6D}(\mathbf{R}) = I_{6D}(\mathbf{R}) + V_{3D}(\mathbf{r_1}) L_{Z_0 \delta Z}(\mathbf{r_1}) + V_{3D}(\mathbf{r_2}) L_{Z_0 \delta Z}(\mathbf{r_2}) \tag{7}$$

for diatomic projectiles, and:

$$V_{3D}(\mathbf{r}) = I_{3D}(\mathbf{r}) + \sum_{j=1}^{m_a} \sum_{i=1}^{n_a} V_{1D}^{j}(\mathbf{r_i}) L_{Z_0 \delta Z}(\mathbf{r_i}) \tag{8}$$

for atomic projectiles. In both cases $L_{Z_0 \delta Z}(\mathbf{r_2})$ is written as:

$$L_{Z_0 \delta Z}(\mathbf{r}_i) = \left[1 + \left(exp\left[\frac{z_i - z_0}{\delta z}\right]\right)\right]^{-1}. \tag{9}$$

From Figs. 4 (b) and 4 (c), we observe that the modified CRP interpolation method yields very accurate results where the standard CRP fails.

Finally, it is worth pointing out that the accuracy of the interpolation method is measured with respect to a DFT energy data set which has not been used in the interpolation (as shown in Figs. 4 (b) and 4 (c)), that is, the ability of the interpolation

method to properly describe the electronic structure of an atom or molecule/surface system depends on the accuracy of the underlying energy data set used in the interpolation.

2.3 Influence of the van der Waals forces

In the context of H_2 and D_2 interaction with surfaces, at normal (or quasi normal) incidence and low impact energy, it has been shown that chemically accurate results can be obtained within the GGA framework using a specific reaction parameter approach[88]. Furthermore, when chemically accuracy is not met, theoretical results are found to be in qualitative agreement with experiments[87,89–91]. These results seem to indicate that the vdW forces are not called to play a key role in GIFMD. However, for GIFAD, where noble gas atoms, mostly He isotopes, are commonly used as projectiles, the role of vdW forces have been subject of increased interest.

From a general point of view, two main schemes have been proposed to include the effect of vdW forces. In the first scheme, vdW effects are taken into account through the inclusion of an additional term (E_D), more or less *elaborate*, in the expression of the self-consistent Kohn-Sham energy (E_{DFT}) of the system, i.e., $E_{DFT+D} = E_{DFT} + E_D$. To this framework belong the correction terms proposed by Grimme and Co.[92–94], Steinman and Co.[95,96], Hafner and Co.[97], and Tkatchenko and Co.[98–100]. This latter family of correction terms[99,100] includes the many-body collective response of the substrate electrons. In the second scheme, new exchange-correlation functionals (E_{xc}) are developed, often *ad-hoc*, adding a nonlocal electron correlation function (E_c^{nl}) to a GGA exchange-correlation functional (E_{xc}^{GGA}), so that $E_{xc} = E_{xc}^{GGA} + E_c^{LDA} + E_c^{ml}$ (see Refs.[101–105] for more details). The use of these latter vdW functionals have been more limited, on the one hand, due to their computational cost, although thanks to the development of efficient algorithms[106] it is now possible to extremely reduce the computational time. On the other hand, because the form of the response function used to compute E_c^{nl} is subject to controversy[107–109].

In the context of GIFAD, the influence of vdW forces has been analyzed for H(D), He and Ne projectiles. In the case of He projectiles, the effect of vdW was discussed, based on indirect evidences, for GIFAD from the $\beta_2(2\times4)$ phase of a GaAs(001) surface[20]. This study showed that for intermediate and high perpendicular incidence energies (>30 meV), diffraction simulations based on a standard DFT-GGA (no vdW included) potential are able to account pretty well for the diffraction charts measured experimentally, which involve a highly corrugated surface with a large number of diffraction channels opened. Whereas in the case of lower energies (<30 meV), where vdW forces are expected to play a more prominent role, the standard DFT-GGA potential overestimates the physisorption potential well, but a simple rescaling of the attractive part of this potential allows one to obtain diffraction charts in good agreement with the experiment, as shown in Fig. 5. Since this rescaling does not affect the results for high normal energies, it might be related to the effect of vdW forces. Thence, this study seems to indicate that for He GIFAD from highly corrugated surfaces, vdW forces only have a measurable effect at very low normal incidence energy.

A direct analysis of the vdW influence on He GIFAD has been performed on He/KCl(001)[85]. In this case, it has been also shown that vdW plays a minor role on diffraction charts for perpendicular incidence energies higher than 30 meV. This conclusion was drawn from the quite good agreement between diffraction charts obtained from theoretical simulations based on a DFT-GGA PES, and those obtained experimentally. In Fig. 6, we show, as an example, theoretical and experimental results for the isotope ^{3}He. From this figure we can also see that the simulated diffraction charts worsen when dynamics calculations are carried out on a vdW-DF2 PES, i.e., a PES obtained from DFT calculations where vdW forces are taken into account throught the functional developed by Langreth and Co.[102]. Weather this result is due to the minor role played by vdW forces or to inaccuracies in the vdW-DF2 functional, which, on the other hand, has shown to yield very good results for diffraction of noble gas atoms from metal surfaces[111], is still under debate.

To enrich the discussion, for the ^{4}He isotope at low normal energies, it has been found that vdW plays a minor role, if any, for incidence along the [110] crystallographic direction[17,113]. From Fig. 7, we observed that the corrugation felt by the ^{4}He projectile, as a function of the perpendicular incidence energy, as well as the rainbow angle, barely depend on the functional, and that, generally speaking, the agreement with the experiment does not improve when vdW forces are considered. In fact, the striking and counter-intuitive increase ($\gtrsim 85\%$) of the corrugation and the rainbow at middle He$-surface$ distances (Z) can be attributed to the combination of soft potential effects and the evolution with Z of the He-cation and He-anion interactions[17]. In contrast, for incidence along the [100] channel with low normal energies, the inclusion of vdW forces seems to improve the agreement between theory and experiment for both the rainbow angle and the corrugation of the PES[55], two physical quantities that probe different regions of the physisorption well. Concerning the influence of the crystallographic direction on vdW effects, we should point out that for alkali-halide surfaces, like KCl(001) or LiF(001), the projectile polarization plays an important role for incidence along the [110] direction because the atom moves along *pure* cation or anion rows. But the polarization contribution becomes negligible for the [100] channel, where the axial rows are formed by alternate negative and positive crystal ions, leading to a null averaged charge of these rows[114]. Hence, this fact should favor the observation of vdW effects along [100] since in this case the weak vdW interaction is not hidden by the more relevant polarization term[55].

The influence of vdW effects has also been analyzed for atomic hydrogen. In this case, it has been shown[84] that for the H/LiF(001) system the description of vdW forces is essential to reproduce experimental GIFAD results for perpendicular incidence energies ≤ 0.5 eV along the crystallographic direction [100], whereas for other incidence conditions vdW forces seem to be negligible[84,115]. VdW forces has been estimated to be also negligible for D/KCl(001)[85], although in this case a more detailed and thorough comparison with experimental data would be needed to validate these conclusions.

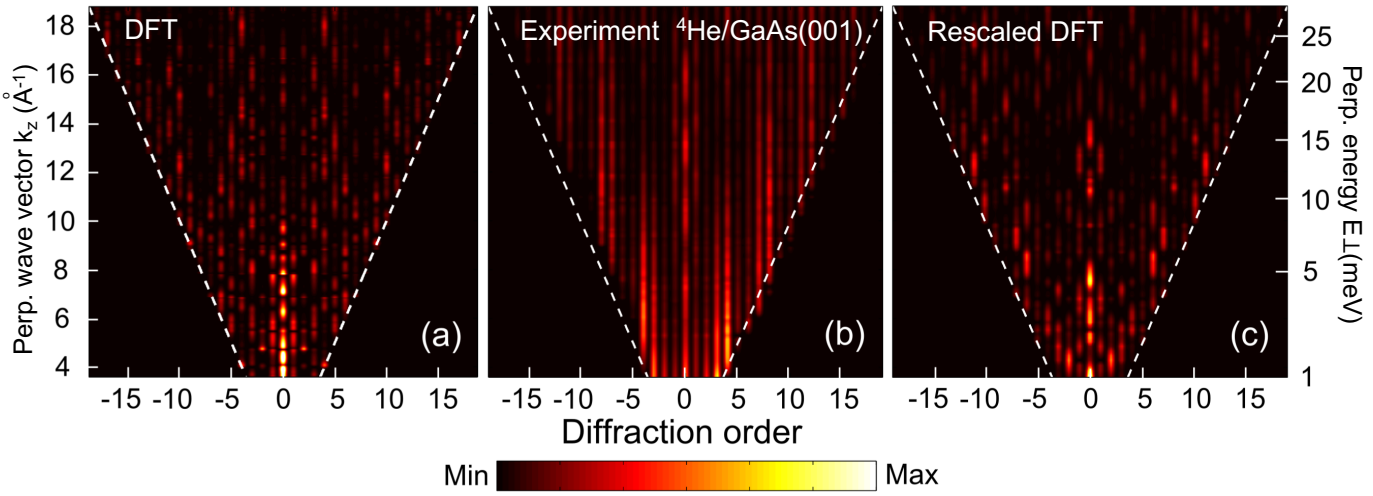

Fig. 5 (Color online) Diffraction charts for ^{4}He atoms incident along the $[1\bar{1}0]$ direction of the $\beta_2(2\times4)$ phase of GaAs(001) at low perpendicular energies. (a) Theoretical simulation obtained directly from DFT; (b) experimental results; (c) theoretical simulation obtained after rescaling of DFT energies. Reprinted with permission from (M. Debiossac, A. Zugarramurdi, H. Khemliche, P. Roncin, A. G. Borisov, A. Momeni, P. Atkinson, M. Eddrief, F. Finocchi, V. H. Etgens, Phys. Rev. B, Combined experimental and theoretical study of fast atom diffraction on the $\beta_2(2\times4)$ reconstructed GaAs(001) surface, **90**, 155308, 2014). Copyright (2014) by the American Physical Society.

At this point, it is worth noting that no functionals have been able to reproduce, with chemical precision, the experimental results for any of the mentioned systems encompassing the entire range of perpendicular incidence energies, regardless of whether vdW is taken into account or not. Therefore, a relevant theoretical challenge within the current context is the improvement of existing DFT functionals, or the development of new ones, in order to adequately describe all physical interactions present in projectile/surface systems, including those due to vdW forces. It is precisely in this task that GIFAD and GIFMD are called to play a very important role because the interference patterns for low normal energies are extremely sensitive to the proper description of the interaction potential. Therefore, GIFAD experiments can be used to test the accuracy of the functionals that can be developed over the next few years with the aim of achieving chemical accuracy in DFT simulations.

3 Grazing incidence fast atoms diffraction (GIFAD)

3.1 Classical methods

Classical dynamics may yield useful outputs related to rainbow angles (Θ_{rb}) in atom-surface scattering[56,116]. But, beyond Θ_{rb} values, classical dynamics simulations can be also used to obtained qualitative information about diffraction-peak probabilities. Although it may well come as a surprise for many that one can study diffraction, the quintessential quantum phenomenon, using classical mechanics, already in the 70's Ray and Bowman showed that the use of a discretization method can make classical trajectory calculations compatible with the Bragg's law[117,118]. According to the Bragg's law, diffraction occurs whenever the variation of the parallel momentum coincides with one of the vectors of the reciprocal lattice. But there is not such a restriction in classical dynamics, where the variation of the parallel momentum can be any vector in the surface reciprocal space. However, if we divide the reciprocal lattice in Wigner-Seitz cells around each lattice point, in such a way that each cell is unambiguously associated with a lattice vector, i.e., with a diffraction peak (see Fig. 8), we can easily assign each classical trajectory with a diffraction peak (n,m) according to the change of its parallel momentum. Thus, the *classical* diffraction probability for a given diffraction peak (n,m) is given by the number of trajectories in which the projectile scatters with a parallel momentum change inside the (n,m) Wigner-Seitz cell, divided by the total number of trajectories. Of course, in this binning method the smaller the Wigner-Seitz cell the more similar the binning to the real parallel momentum change quantization. Although one cannot expect quantitatively accurate results from this classical binning method, the procedure allows one to obtain good trends at a very cheap computational cost. An example of GIFAD results for H/LiF(001) obtained using this simple method is shown in Fig. 9. From this figure, we can see the very good qualitative agreement between the classical simulated diffraction spectrum and the experimental one[11,83].

Note that for the H/LiF(001) system, binning results agree with experimental data[119] even in the stronger corrugation felt by hydrogen atoms diffracted along the [100] direction of the LiF(001) surface, in comparison with those diffracted along the [110] one[83]. The diffraction spectra for H/LiF(001) obtained with the binning method can be understood in terms of the geometrical structure factor (S_g), which can be expressed as a combination of the atomic form factors (F_{Li} and F_F)[83] as:

$$S_g = F_{Li}(\mathbf{G})\, e^{i\mathbf{G}\cdot\mathbf{d}_{Li}} + F_F(\mathbf{G})\, e^{i\mathbf{G}\cdot\mathbf{d}_F}, \qquad (10)$$

where the reciprocal lattice vector ($\mathbf{G}$) is given by $\mathbf{G} = n\mathbf{b}_1 + m\mathbf{b}_2$, with $\mathbf{b}_1$ and $\mathbf{b}_2$ representing the primitive reciprocal lattice vectors, and $\mathbf{d}_{Li}$ and $\mathbf{d}_F$ the atomic basis set vectors. Thus, $S_g = F_{Li} + F_F$ if $n+m$ is an even number, and $S_g = F_{Li} - F_F$ if $n+m$ is an odd number. As it can be seen from Fig. 8, all the

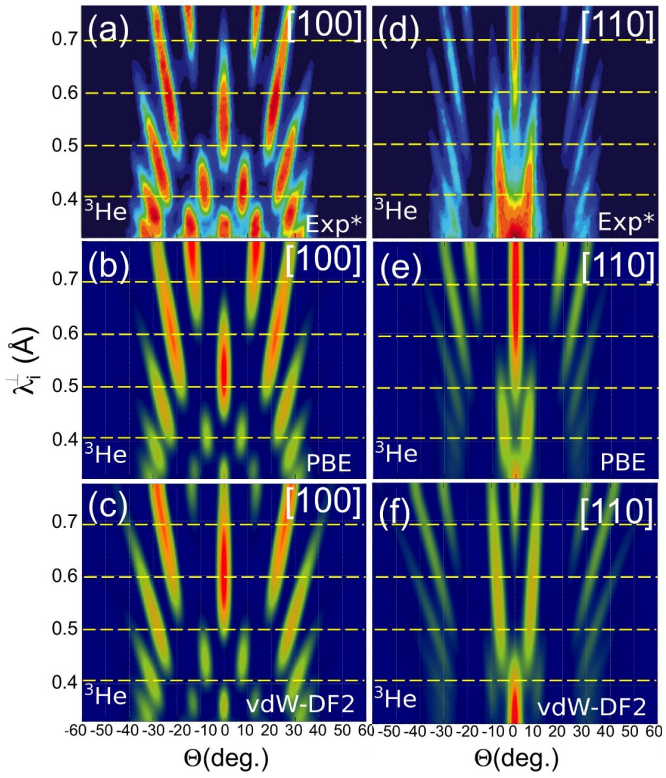

Fig. 6 (Color online) Diffraction spectra of ^{3}He/KCl(001). Top panels (a and d) are the experimental spectra from Ref.[110]: middle panels (b and e) are the simulated theoretical spectra using a DFT-PBE PES; bottom panels (c and f) are the simulated theoretical spectra using a vdW-DF2 PES. Left and right panels correspond to incidence along the [100] and [110] crystallographic directions, respectively. The dashed yellow lines are just to guide the eye. Reprinted from Nucl. Instrum. Meth. Phys. Res. B **476**, 1-9, 2020, M. del Cueto, A. S. Muzas, F. Martín, C. Díaz, Accurate simulations of atomic diffractive scattering from KCl(001) under fast grazing incidence conditions, copyright (2020) with permission from Elsevier.

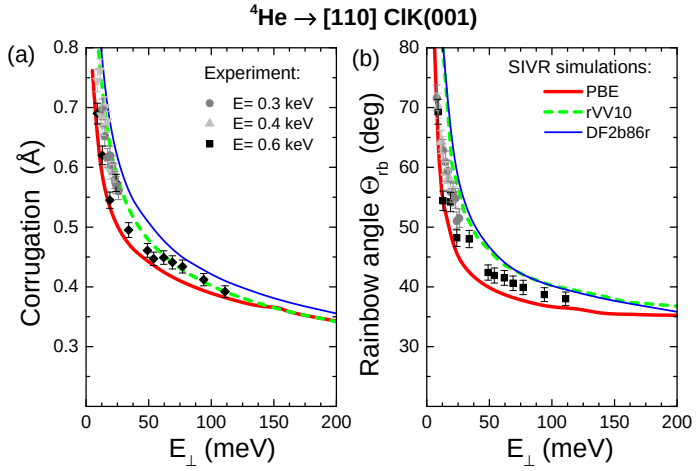

Fig. 7 (Color online) (a) Surface corrugation and (b) rainbow deflection angle, as a function of the normal incidence energy, for ^{4}He → [110] KCl(001) obtained from experiments[17] and SIVR simulations[17] based on three different DFT functionals: PBE[72]; rVV10 (vdW1)[112]; and DF2b86r (vdW2)[104]. Reprinted with permission from (G. A. Bocan, H. Breiss, S. Szilasi, A. Momeni, E. M. Staicu-Casagrande, M. S. Gravielle, R. A. Sánchez, H. Khemliche, Phys. Rev. Lett., Anomalous KCl(001) Surface Corrugation from Fast He Diffraction at Very Grazing Incidence, **125**, 096101, 2020). Copyright (2020) by the American Physical Society.

diffraction peaks observed along the [100] direction correspond to $n + m$ =even, i.e., for all of them $S_g = F_{Li} + F_F$. Whereas along the [110] direction, diffraction peaks with $n+m$ =even and $n+m$=odd alternate. This fact, along with the dependence of the form factors with the corrugation of the PES, explains the stronger peak-modulation observed along the [110] direction.

In addition, the classical binning method could be further improved, without significantly increasing the current very low computational requirements, by incorporating a Gaussian weighting into the binning[120,121].

3.2 Semiclassical approximation

A more refined way of dealing with atom-surface diffraction, but still using a classical description of the projectile motion, is provided by the semiclassical approximations. Semiclassical approaches have played an important role in the understanding of atom and molecule diffraction from surfaces[122–128] over time. This holds also for GIFAD, whose first theoretical prediction[129], some years before the experimental reports[1,2], was based on a semiclassical approximation. Although Ref.[129] remained almost unknown until 2009[9], early articles on GIFAD[114,130,131] made use of semiclassical models to unravel the main physical mechanisms involved in this unexpected phenomenon. Moreover, semiclassical approximations based on 3D classical trajectories, as well as the much simpler Hard-Corrugated Wall (HCW) model[132] that completely neglects soft-potential contributions, were widely employed to extract surface information from GIFAD experiments. Among the former approaches, we can mention semiclassical models that combine classical[18,26,31,130,133] or local classical[20] scattering cross sections, incorporating a phase to take into account the quantum interference, and those derived from the eikonal approach, like the surface eikonal (SE) approximation[9,42,43,82,114] and the semiclassical method developed by Manson and Co.[131].

Concerning these semiclassical approximations for GIFAD[9,18,20,31,43,82,133], we should point out that despite they shown to provide a successful representation of the experimental diffraction patterns, their results largely overestimate the intensity of the outermost maxima of the angular distribution when these peaks are close to the classical rainbow angles. This is a well-known deficiency related to the classical description of the rainbow scattering[134], which introduces a point of accumulation of trajectories with maximum azimuthal deflection, giving rise to cusped rainbow peaks. Instead, projectile distributions obtained from full quantum treatments, as well as from adequate semiclassical calculations, present smooth rainbow maxima with a exponential decrease of the scattering probability outside the classical rainbow angles, in the angular region corresponding to classically forbidden transitions.

On the other hand, it should be also mentioned that although in many cases the simple HCW model has proved to give a good

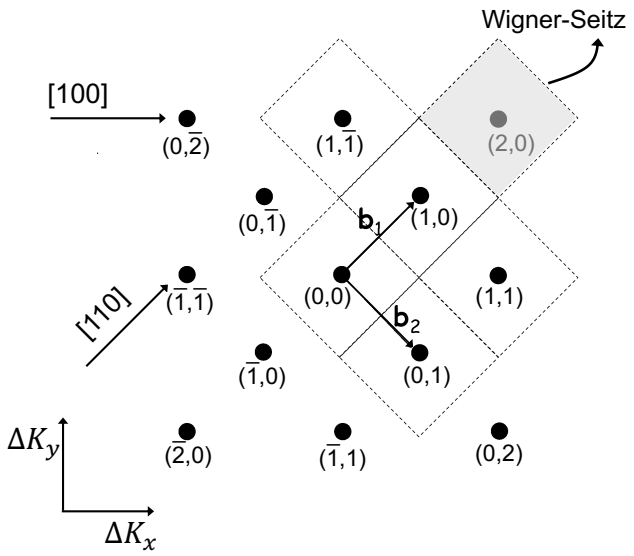

Fig. 8 (Color online) Reciprocal lattice corresponding to LiF(001). The dotted lines delineate the 2D Wigner-Seitz cells around each lattice point. The numbers within parentheses indicate the diffraction peaks; numbers within brackets indicate the two main crystallographic directions.

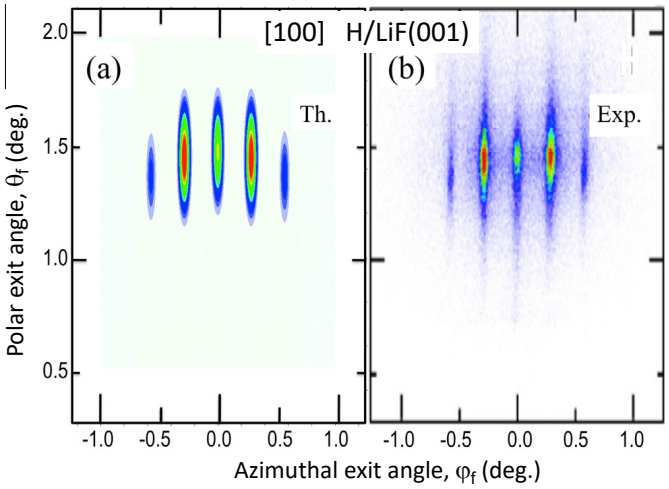

Fig. 9 (Color online) (a) 2D classically simulated diffraction spectrum for H/LiF(001) along the incidence direction [100] for total incidence energy of 0.9 keV and incidence angle of 1.48°; (b) The corresponding experimental spectrum[11]. Note: The theoretical results have been convoluted with a 2D Gaussian function of width $\sigma_\varphi = 0.025°$ and $\sigma_\theta = 0.12°$ to simulate the experimental spread. Reprinted from Nucl. Instrum. Meth. Phys. Res. B **354**, 9-15, 2015,A. S. Muzas, F. Martín, C. Díaz, Scattering of H(D) from LiF(100) under fast grazing incidence conditions: To what extent is classical dynamics a useful tool?, copyright (2015) with permission from Elsevier.

representation of the intensity modulation of the experimental GIFAD patterns[24,27–29,135], such a description is associated with effective parameters of the real soft atom-surface potential, whose effects should be taken into account in order to use GIFAD as a surface analysis technique[26,133]. Notice that these soft potential effects are particularly important for GIFAD at low normal energies[17,55].

In this context, the surface initial value representation (SIVR) approximation[44] was developed in order to solve the rainbow weakness of previous semiclassical models. The SIVR approach is a semiquantum method for grazing atom-surface scattering that takes into account quantum effects, such as interference, coherence lengths, and classically forbidden transitions, without losing the appealing representation of the interference mechanisms in terms of classical trajectories. This approximation is based on the IVR approach by W. H. Miller[136], which has been extensively employed to investigate different atomic, molecular and nuclear processes[136–142]. Within the framework of the Feynman path integral formulation of quantum mechanics, the IVR model replaces the exact quantum time-evolution operator with its Van Vleck approximated version[143] in terms of classical paths, which is numerically evaluated without incorporating additional simplifications. Hence, this IVR time-evolution operator represents a practical way of avoiding the classical rainbow divergence.

The SIVR model[44,144] makes use of the IVR time-evolution operator within a full quantum distorted-wave formalism[145], giving rise to the transition amplitude $A^{(SIVR)}$ that includes, albeit in an approximated way, classically forbidden contributions on the dark side of the classical rainbow angle. For the elastic scattering $\mathbf{K}_i \to \mathbf{K}_f$, with $\mathbf{K}_i$ ($\mathbf{K}_f$) being the initial (final) projectile momentum and $K_i = K_f$, the SIVR transition amplitude reads

$$A^{(SIVR)} = \int d\mathbf{r}_o \; f_s(\mathbf{r}_o) \int d\mathbf{k}_o \; f_m(\mathbf{k}_o) \; a^{(SIVR)}(\mathbf{r}_o, \mathbf{k}_o), \qquad (11)$$

where

$$a^{(SIVR)}(\mathbf{r}_o, \mathbf{k}_o) = \int_0^{+\infty} dt \;\; [J_M(t)]^{1/2} V(\mathbf{r}_t) \exp\left[i \left(\phi_t^{(SIVR)} - \mathbf{Q} \cdot \mathbf{r}_o \right) \right] \qquad (12)$$

is, except for a constant factor, the partial transition amplitude associated with the classical projectile path $\mathbf{r}_t \equiv \mathbf{r}_t(\mathbf{r}_o, \mathbf{k}_o)$, with $\mathbf{r}_o$ and $\mathbf{k}_o$ being the starting position and momentum, respectively, at the time $t = 0$. The Maslov function $J_M(t) = \det[\partial \mathbf{r}_t(\mathbf{r}_o, \mathbf{k}_o)/\partial \mathbf{k}_o]$ (a determinant) takes into account the correlation among nearby trajectories, $\mathbf{Q} = \mathbf{K}_f - \mathbf{K}_i$ is the momentum transfer, and $\phi_t^{(SIVR)}$ denotes the SIVR phase along the trajectory:

$$\phi_t^{(SIVR)} = \int_0^t dt' \; \left[\frac{1}{2m_P} \left(\mathbf{K}_f - \mathbf{k}_{t'} \right)^2 - V(\mathbf{r}_{t'}) \right], \qquad (13)$$

with $\mathbf{k}_t = m_P d\mathbf{r}_t/dt$ being the time-dependent classical momentum and m_P the projectile mass.

In Eq. (11) the functions $f_s(\mathbf{r}_o)$ and $f_m(\mathbf{k}_o)$ describe the spatial and momentum profiles, respectively, of the initial coherent wave packet at a fixed distance z_o from the surface where the time evolution is started. Then, the transition amplitude $A^{(SIVR)}$ contains the interference among different partial amplitudes $a^{(SIVR)}$ associated with a given incident wave packet, which is the ultimately origin of the quantum interference effects. From the SIVR transition amplitude, given by Eq. (11), the differential scattering probability in the direction of the solid angle $\Omega_f \equiv (\theta_f, \varphi_f)$ is

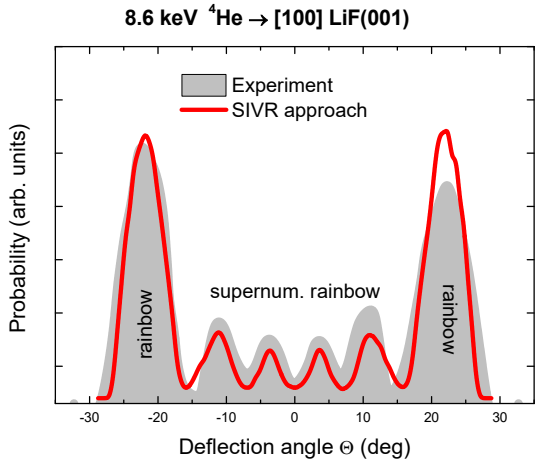

Fig. 10 (Color online) Intra-channel distribution, as a function of the deflection angle Θ, for ^{4}He atoms scattered from LiF(001) along the [100] direction with $E = 8.6$ keV and $\theta_i = 0.71$ deg. Solid red line, SIVR results for the intra-channel mechanism (i.e., for $N = 1$) extracted from Ref.[44]; shadow gray line, experimental data from Ref.[130].

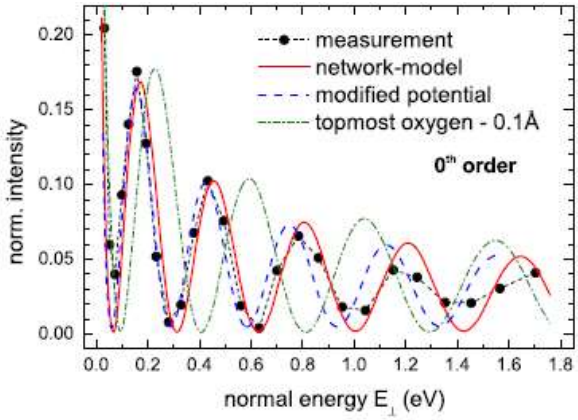

Fig. 11 (Color online) Normalized peak intensity of the 0^{th} Bragg order, as a function of the normal energy $E_\perp$, for ^{4}He atoms scattered along the [01] direction of a monolayer silica film on Mo(112). Reprinted with permission from (J. Seifer, A. Schüller, H. Winter, R. Wlodarczyk, J. Sauer and M. Sierka, Phys. Rev. B, Diffraction of fast atoms during grazing scattering from the surface of an ultrathin silica film on Mo(112), **82**, 035436, 2014). Copyright (2014) by the American Physical Society.

obtained as $dP^{(SIVR)}/d\Omega_f = K_f^2 \left|A^{(SIVR)}\right|^2$.

By using the SIVR approximation, it is possible to analyze the different interference mechanisms involved in GIFAD. Like in any interference phenomenon from a periodic grating, GIFAD patterns are determined by two different mechanisms - inter- and intra-channel interferences - associated respectively with Bragg diffraction and supernumerary rainbows[130]. Within the SIVR approach, each of these mechanisms corresponds to a different factor of the transition amplitude, that is,

$$A^{(SIVR)} = S_N \, A_{N=1}^{(SIVR)}, \tag{14}$$

where S_N is the inter-channel factor produced by interference among parallel channels, which presents a closed form depending on both the transverse spacial periodicity a_y of the crystal and the number N of equivalent parallel channels that are coherently illuminated by the incident wave packet. In turn, the intra-channel factor $A_{N=1}^{(SIVR)}$ corresponds to the transition amplitude for a single-channel illumination[44]. Hence, S_N represents a geometrical structure factor that gives rise to Bragg maxima, whose relative intensities are modulated by $A_{N=1}^{(SIVR)}$, which acts as an enveloped function that presents rainbow and supernumerary rainbow maxima[130], as displayed in Fig. 10.

Since the intra-channel structures are strongly sensitive to the interaction potential, the relative intensities of the Bragg peaks[15,29,31,133,146], or alternatively, rainbow and supernumerary rainbow maxima[9,43], are commonly used to extract detailed surface information from GIFAD experiments. For example, in Fig. 11 the intensity of the central peak (0^{th} Bragg order) derived from a simpler semiclassical model is used to investigate the structure of a monolayer silica film grown on Mo(112)[31], while in Fig. 12 supernumerary rainbow positions derived from the SIVR approach are compared with experimental data in order to probe the PA potentials displayed in Fig. 3, checking the contribution of the electron correlation term[41].

Furthermore, semiclassical methods can be used as a tool to investigate the coherent and incoherent contributions to GIFAD, as discussed in the following subsections.

3.2.1 Projectile coherence

In matter-wave optics[147], like in light optics, the coherence properties of the wave play a central role in the interference effects. In particular, the collimating conditions of the incident beam are critical for matter interferometry involving heavy particles, like atoms or molecules, because the observation of quantum interference strongly depends on the relation between the projectile coherence length and the grating parameters[148–151]. This issue was extensively investigated for atomic diffraction from surfaces at thermal energies[6,152,153], but in the case of GIFAD, Ref.[154] is, to our knowledge, the unique experimental study on the influence of the beam collimation on diffraction patterns. In that article[154], angular distributions for 1 keV He atoms scattered off a LiF(001) surface under different collimating conditions are reported, displaying a pronounced dependence on the width of the collimating slit (see top panels of Fig. 13).

From the theoretical point of view, the degree of coherence of the atomic beam determines the dimensions of the initial coherent wave packet[144,155], which depend not only on the collimating setup but also on the characteristics of the atom source and the incidence conditions. Within the SIVR approach, the spatial profile of the initial wave packet at a distance z_o from the surface where the time evolution is started (usually chosen as equal to the lattice constant) is given by the complex degree of coherence[156] ($\mu_{coh}(\mathbf{r}_{o\|})$) of the atomic beam as $\left|f_s(\mathbf{r}_{o\|})\right|^2 = \left|\mu_{coh}(\mathbf{r}_{o\|})\right|^2$, with $\mathbf{r}_{o\|} = x_o\hat{\mathbf{x}} + y_o\hat{\mathbf{y}}$ being the component of the starting position parallel to the surface plane. By assuming an atomic beam produced

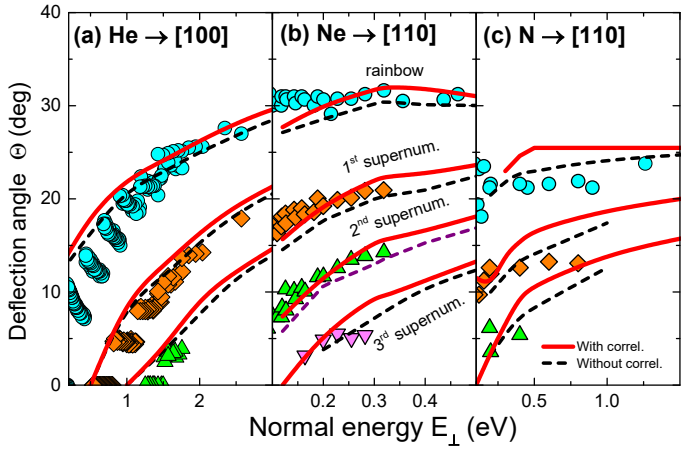

Fig. 12 (Color online) Deflection angles Θ corresponding to rainbow and supernumerary rainbow maxima, as a function of the normal energy $E_\perp$, for ^{3}He atoms scattered along [100] (left), and for Ne (middle) and N (right) atoms impinging along the [110] direction. In all panels, red solid (black dashed) line, SIVR rainbow and supernumerary rainbow angles derived with (without) the inclusion of correlation in the PA model (see Sec. 2.1). Symbols: experimental data extracted from Refs.[9,41,43]. Reproduced from Ref.[36] with permission from World Scientific, copyright 2019.

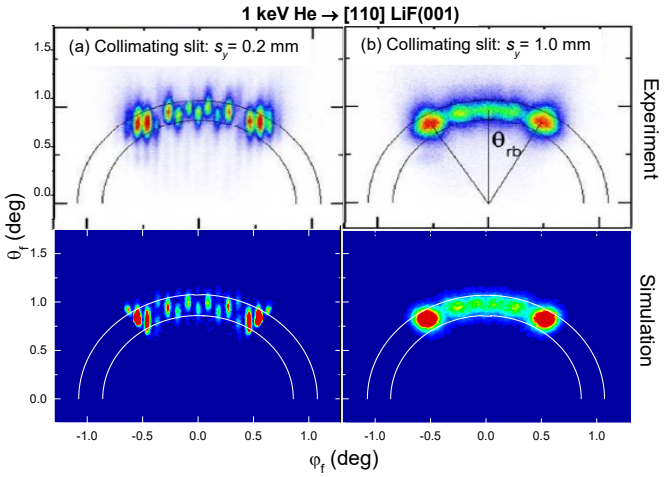

Fig. 13 (Color online) Projectile distribution, as a function of the final dispersion angles θ_f and φ_f , for 1 keV ^{4}He atoms impinging on LiF(001) along the [110] direction with the incidence angle $\theta_i = 0.99$ deg. Two different widths of the collimating slit, placed at $L = 25$ cm, are used: (a) $s_y = 0.2$ mm and (b) $s_y = 1.0$ mm. Top panels, experimental distributions extracted from Ref.[154]; bottom panels, SIVR distribution taken from Ref.[144]. Reprinted with permission from (M. S. Gravielle, J. E. Miraglia, Phys. Rev. A, Influence of beam collimation on fast-atom diffraction studied via a semiquantum approach, **92**, 062709, 2015). Copyright (2015) by the American Physical Society.

by an extended incoherent quasi-monochromatic source, passing through a rectangular collimating slit placed perpendicular to $\mathbf{K}_i$ at a long distance from the surface and the source, the complex degree of coherence can be derived from the Van Cittert-Zernike theorem as[157]:

$$\left|\mu_{coh}(\mathbf{r}_{o\parallel})\right|^2 \simeq j_0^2\left(\frac{\pi s_x}{\lambda_\perp L}x_o\right) j_0^2\left(\frac{\pi s_y}{\lambda L}y_o\right), \tag{15}$$

where $j_0(x)$ is the spherical Bessel function, L is the distance of the collimating slit to the surface, and s_x and s_y denote the lengths of the sides of the rectangular collimating aperture. From Eq. (15), $f_s(\mathbf{r}_{o\parallel})$ can be approximated as a product of Gaussian functions:

$$f_s(\mathbf{r}_{o\parallel}) \simeq G(\sigma_x, x_o) G(\sigma_y, y_o), \tag{16}$$

where $G(\omega, x) = [2/(\pi\omega^2)]^{1/4} \exp(-x^2/\omega^2)$ and

$$\sigma_x = \frac{\lambda_\perp}{\sqrt{2}}\frac{L}{s_x}, \quad \sigma_y = \frac{\lambda}{\sqrt{2}}\frac{L}{s_y}. \tag{17}$$

are the corresponding *transverse* coherence lengths, which determine the spatial size of the coherent wave packet at a distance z_o from the surface.

On the other hand, the *longitudinal* coherence length[149] does not play any role in typical GIFAD experiments because the atomic beam presents a well defined energy (i.e., $\Delta E/E \ll 1$)[154,158]. Thence, the starting momentum $\mathbf{k}_o$ satisfy the energy conservation, with $k_o = \sqrt{2m_P E}$, reducing the momentum profile of the initial wave packet to an angular distribution:

$$f_m(\mathbf{k}_o) \simeq f_m(\Omega_o) = G(\sigma_\theta, \theta_o - \theta_i) G(\sigma_\varphi, \varphi_o), \tag{18}$$

where $\Omega_o \equiv (\theta_o, \varphi_o)$ is the solid angle corresponding to the $\mathbf{k}_o$ direction and the angular widths $\sigma_\theta = \lambda_\perp/(2\sigma_x)$ and $\sigma_\varphi = \lambda/(2\sigma_y)$ are derived from the uncertainty principle[159].

From Eqs. (16) and (17) it is clear that the size of the collimating aperture affects the surface region coherently illuminated by the projectile wave packet, allowing one to control the mechanisms that govern the GIFAD pattern. In fact, the key parameter in the simulations of Fig. 13 is the number N of equivalent parallel channels (with width a_y) that are coherently illuminated by the atomic beam, which can be estimated as[160]

$$N \simeq \frac{2\sigma_y}{a_y} = \frac{L}{s_y}\frac{2\pi}{a_y\sqrt{m_P E}}\,. \tag{19}$$

For the collimating slit with $s_y = 0.2$ mm [Fig. 13 (a)], the atomic beam coherently illuminates about $N \simeq 3$ channels, giving rise to a projectile distribution with well defined Bragg peaks, in agreement with the experimental pattern. But when s_y increases, the value of N decreases, and consequently, the width of the Bragg peaks gradually increases. For $s_y = 1.0$ mm [Fig. 13 (b)], $N \lesssim 1$ leads to cancellation of the inter-channel interference and the simulated distribution only displays supernumerary rainbow structures associated with $A_{N=1}^{(SIVR)}$, as it is also observed in the experiment.

A similar effect is found by varying the impact energy since N decreases as E increases[160], as given by Eq. (19). Furthermore, when σ_y becomes smaller than the channel width (i.e., $N < 1$), it is necessary to include the spot-beam contribution due to different microscopic positions of the focus point of the atomic beam[161]. Each of them probes a different local zone of the atom-surface potential inside a single channel, introducing an incoherent background that reduces the visibility of the intra-channel structures.

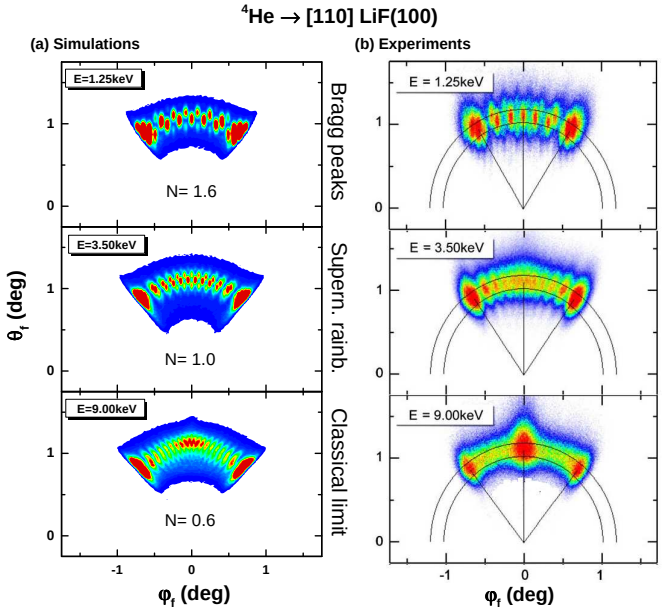

Fig. 14 (Color online) Projectile distributions, as a function of θ_f and φ_f, for ^{4}He atoms impinging on LiF(001) along [110] with $\theta_i = 1.1$ deg. (a) (left panels) Simulated SIVR results derived by considering a collimating slit of width $s_y = 0.3$ mm, placed at $L = 25$ cm; (b) (right panels) experimental distributions extracted from Ref. [10]. In both columns, different impact energies - $E = 1.25$, 3.50, and 9.00 keV - are considered. The corresponding N values, as given by Eq. (19), are indicated. Reproduced from Ref. [161] with permission from the institute of physics, copyright 2018.

This makes the projectile distribution tend to the classical limit at high energies, as shown in Fig. 14. In an analogous fashion, inelastic scattering processes are expected to contribute to wash out the interference patterns as the normal energy increases (see Fig. 16 of Ref. [12]).

Finally, notice that despite all the projectile distributions of Figs. 13 and 14 lay inside an annulus of mean radius θ_i as a consequence of the energy conservation [1,2], the spectra display elongated structures. The length of such vertical streaks is affected by the length s_x of collimating slit [144,157] through σ_θ, as well as by phonon-mediated processes, among other expected contributions [12]. This question will be discussed in detail in Sec. 3.2.4

3.2.2 Decoherent contributions

In Sec. 3.2.1, we have analyzed the influence of the coherence of the incident beam in GIFAD patterns. However, the observation of quantum interference also depends on the coherence properties of both the crystal target and the scattering mechanism. Regarding the latter issue, first GIFAD experiments [1,2] made use of insulator surfaces, for which electronic excitations were expected to be strongly suppressed due to the presence of a wide band gap [155]. This fact was experimentally verified for the He/LiF(001) system [162]. But for hydrogen projectiles, measurements in coincidence with energy-loss detection showed that in this case the electronic excitations introduce an incoherent background into the elastic distributions, which are governed by quantum interference [13,162]. A similar inelastic background was also predicted for metal surfaces, like Ag(110), for which well defined GIFAD patterns were observed [24,82] despite the decoherent effect of electronic transitions [163], as it will be discussed in Sec. 3.2.5.

But in addition to electron excitations, there are other scattering mechanisms that are foreseen to affect the coherence, like those involving crystal lattice vibrations, i.e., phonons, which were early suspected of playing an important role in GIFAD from insulating surfaces [155]. Particularly, thermal lattice vibrations, because most of the GIFAD experiments were carried out with crystal targets at room temperature, whose mean thermal lattice fluctuations are usually larger than the de Broglie wavelengths of the incident projectiles [131,155]. However, GIFAD experiments for a huge variety of materials, not only at room temperature but also at much higher temperatures [34], promptly proved that the quantum interference prevails over thermal decoherence, making possible to use GIFAD to measure surface parameters smaller than thermal vibration amplitudes, like the rumpling of the topmost surface layer [133,146]. In the next subsection we will focus on the contribution of phonon-mediated scattering.

3.2.3 Phonon-mediated scattering

In spite of the intense experimental work on GIFAD developed over the past 15 years, the theoretical study of the contribution of phonon-mediated processes has had a slower progress. In the literature, the vast majority of GIFAD descriptions are based on elastic scattering from an ideal and frozen crystal surface, leaving aside the effect of thermal lattice vibrations. On the contrary, the decoherence introduced in GIFAD by phonon-mediated scattering was scarcely studied in early works [131,146,155,164]. Even though this is an important question for the use of GIFAD as a surface analysis tool, it has only recently received renewed attention [37–40,165,166], representing a problem not fully understood yet.

Among these recent theoretical developments that include lattice vibrations, we can mention the phonon-surface initial value representation (P-SIVR) approximation [38], which is an extension of the SIVR approach (summarized in Sec. 3.2) in order to incorporate phonon transitions. It is done by replacing the rigid-surface description with a quantum representation of the surface given by the harmonic crystal model [50]. Within the P-SIVR method [38], the classical trajectories $\mathbf{r}_t$ depend also on the spatial configuration of the crystal at $t = 0$, which is determined by the $3N_c$-dimension vector $\underline{\mathbf{u}}_o$ associated with the 3D displacements of the N_c ions contained in the crystal sample, with respect to their equilibrium positions. By using PA potentials, the P-SIVR probability can be expressed as a series on the number n of phonons emitted or absorbed during the collision, where each Pn-SIVR probability is associated with grazing scattering involving the net exchange of n phonons. The zero-order term,

$$dP^{(P0-SIVR)}/d\Omega_f = K_f^2 \left| \mathscr{A}_{n_{ph}=0} \right|^2, \qquad (20)$$

corresponds to elastic scattering without net phonon exchange

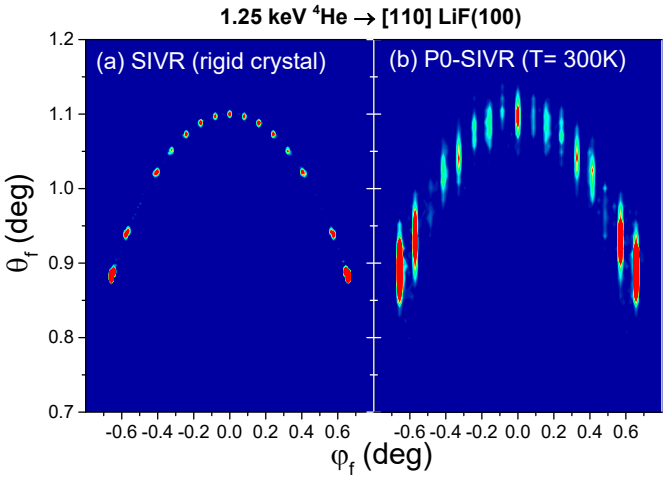

Fig. 15 (Color online) Projectile distributions, as a function of θ_f and φ_f, for 1.25 keV ^{4}He atoms scattered off LiF(001) at the temperature $T = 300$ K, with $E_\perp = 0.46$ eV. Results derived within (a) the SIVR approximation, for a rigid crystal, and (b) the P0-SIVR approach, including thermal vibrations, are displayed. Reprinted with permission from (I.Frisco, M. S. Gravielle, Phys. Rev. A, Thermal effects on helium scattering from Lif(001) at grazing incidence, **102**, 062821, 2020). Copyright (2020) by the American Physical Society.

(i.e., $n_{ph} = 0$), while the first-order term,

$$dP^{(P1-SIVR)}/d\Omega_f = K_f^2 \sum_{\mathbf{k},l} \left[\frac{N_l(\mathbf{k})}{\omega_l(\mathbf{k})} \left| \mathscr{A}_{n_{ph}=-1}(\mathbf{k},l) \right|^2 + \frac{N_l(\mathbf{k})+1}{\omega_l(\mathbf{k})} \left| \mathscr{A}_{n_{ph}=+1}(\mathbf{k},l) \right|^2 \right], \quad (21)$$

describes the one-phonon scattering, where $\mathscr{A}_{n_{ph}}$ is the effective transition amplitude for n_{ph} phonons emitted ($n_{ph} = -n$) or absorbed ($n_{ph} = +n$) by the crystal during the collision. In Eq. (21) the sum runs over the different normal modes of the crystal, with $\omega_l(\mathbf{k})$ being the phonon frequency in the branch l, with the wave vector $\mathbf{k}$, and $N_l(\mathbf{k}) = (\exp[\omega_l(\mathbf{k})/(k_B T)] - 1)^{-1}$ is the Bose-Einstein occupation function for $(\mathbf{k}, l)$ phonons in a crystal at temperature T, with k_B being the Boltzmann constant. The complete expression of $\mathscr{A}_{n_{ph}}$ is given in Eq. (3) of Ref.[38] and involves the addition (that is, the integral) of all possible spatial configurations $\underline{\mathbf{u}}_o$ of the crystal lattice.

While Eq. (21), associated with inelastic phonon-mediated scattering, is still pending numerical evaluation, the probability P0-SIVR [Eq. (20)], which allows one to investigate the effect owing to thermal lattice vibrations, was evaluated for different collision systems[38,39]. It can be expressed in terms of partial transition amplitudes obtained from Eq. (12) by replacing the potential along the trajectory with an effective potential (i.e., a crystal factor) that reads:

$$\mathscr{V}_0(\mathbf{r}_t) = \int d\mathbf{q} \sum_{\mathbf{r}_B} \tilde{v}_{\mathbf{r}_B}(\mathbf{q}) \exp[-W_{\mathbf{r}_B}(\mathbf{q})] \times \exp[i\mathbf{q}\cdot(\mathbf{r}_t - \mathbf{r}_B)], \quad (22)$$

where $\tilde{v}_{\mathbf{r}_B}(\mathbf{q})$ denotes the Fourier transform of the binary interaction between the projectile and the crystal ion placed at the Bravais position $\mathbf{r}_B$, $W_{\mathbf{r}_B}(\mathbf{q}) = \left\langle [\mathbf{q}\cdot\mathbf{u}(\mathbf{r}_B)]^2 \right\rangle / 2$ is the usual momentum-dependent Debye-Waller function, with $\mathbf{u}(\mathbf{r}_B)$ the displacement of the crystal ion at $\mathbf{r}_B$, and the sum covers all the occupied lattice sites. In this way, within the transition amplitude $\mathscr{A}_{n_{ph}=0}$ thermal effects result included through two different contributions: *i)* the coherent contribution of classical projectile trajectories produced by different spatial configurations $\underline{\mathbf{u}}_o$ of the crystal, and *ii)* the effective screening of the potential along each projectile path due to the exponential Debye-Waller factor, which takes into account the incoherent sum over all the intermediate phonon excitations (i.e., the addition of the square modulus of the partial crystal transition amplitudes). In contrast, early works on GIFAD[146,155] include the contribution of lattice vibrations by averaging the transferred momentum by binary collisions[155] or the surface potential[146] over randomly displaced positions of the crystal ions.

To illustrate the performance of the P0-SIVR approximation, in Fig. 15 the projectile distribution for zero-phonon scattering, derived from Eq. (20), is contrasted with that obtained within the SIVR approach for a rigid surface, using He/LiF(001) at room temperature as a benchmark system[39]. From this figure, it is clear that the effect of thermal lattice fluctuations contributes to the formation of elongated strips, feature also observed in GIFAD experiments. Furthermore, the positions of the Bragg peaks are not affected by the lattice vibrations, although depending on the normal energy, their relative intensities are. In fact, thermal effects can even lead to the appearance of sub-patterns of interference as a function of the polar angle, like the ones observed in Fig. 16. In this figure, the intra-channel distribution for Ne impact on LiF(001) at room temperature shows an additional polar pattern in the central region, which gives rise to doubly peaked structures in the azimuthally-projected spectrum[38]. A more quantitative evaluation of the contribution of thermal fluctuations within the P0-SIVR approach can be obtained from the contrast of the azimuthal spectra corresponding to the cases of Figs. 15 and 16, which are respectively displayed in Fig. 4 of Ref.[39] and Fig. 3 of Ref.[38]. At this point, it should be recalled that such thermal effects in GIFAD patterns were already predicted in a pioneer article by Manson and Co.[131].

Furthermore, P0-SIVR simulations indicate that the interference structures might be still visible for LiF(001) surfaces at temperatures up to $T \simeq 600$ K, starting to blur out for higher temperatures[39]. Although this thermal behavior is in agreement with GIFAD experiments for GaAs surfaces, where the interference patterns were used to monitor the layer-by-layer grow[34] at temperatures as high as 620 ^{o}C, these findings for the prototype system He/LiF(001) would require future experimental research.

3.2.4 Polar-angle profile

As mentioned above, the most striking characteristic introduced by lattice vibrations is the polar elongation of the interference patterns, which transforms the circular spots corresponding to elastic scattering from an ideal rigid surface into vertical strips, as observed experimentally (see Figs. 13 and 14). However, we should point out that it has not been possible yet to accurately

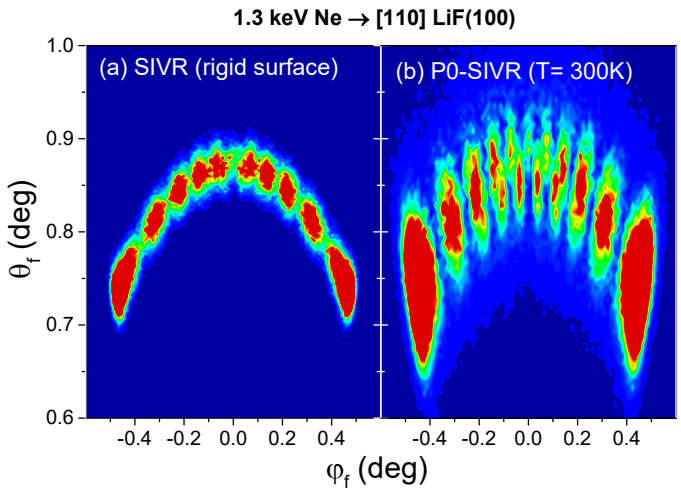

Fig. 16 (Color online) Intra-channel distribution, as a function of θ_f and φ_f, for 1.3 keV Ne atoms scattered off LiF(001) at the temperature $T = 300$ K, with $E_\perp = 0.30$ eV. Reprinted with permission from (I.Frisco, M. S. Gravielle, Phys. Rev. A, Phonon contribution in grazing-incidence fast atom diffraction from insulator surfaces, **100**, 062703, 2019). Copyright (2019) by the American Physical Society.

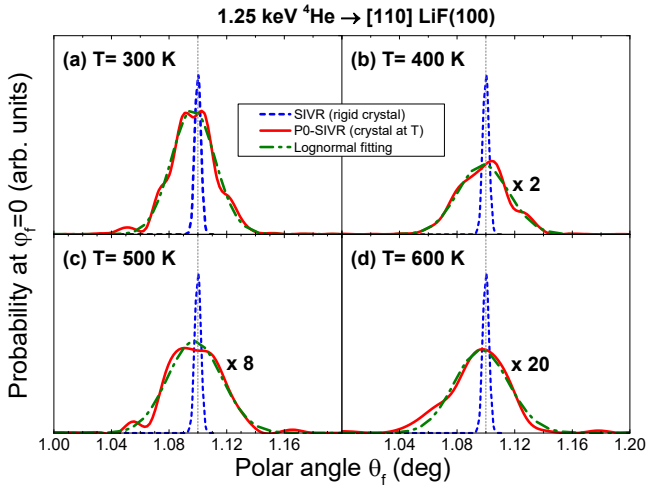

Fig. 17 (Color online) Intensity profile of the central maximum at $\varphi_f = 0$, as a function of the polar angle θ_f, for the case of Fig. 15, considering different temperatures: (a) $T = 300$ K, (b) $T = 400$ K, (c) $T = 500$ K, and (d) $T = 600$ K. In all the panels, red solid line, differential probability derived within the P0-SIVR approach; blue dashed line, SIVR probability for a rigid crystal; green dot-dashed line, fitting of P0-SIVR results by means of a lognormal distribution, as given by Eq. (23). Vertical gray dashed line, ideal θ_f- position on the Laue circle (i.e., $\theta_f = \theta_i$). Reprinted with permission from (I.Frisco, M. S. Gravielle, Phys. Rev. A, Thermal effects on helium scattering from Lif(001) at grazing incidence, **102**, 062821, 2020). Copyright (2020) by the American Physical Society.

reproduce the experimental polar distributions by means of *ab initio* models without the inclusion of parameters *ad hoc*. Thus, the study of the polar profiles in GIFAD has became a problem of great interest, being the focus of recent works[39,40].

For the He/LiF(001) system at different temperatures T, in Fig.17 we show the polar profile of the central maximum derived from the P0-SIVR approach, along with the SIVR polar distribution for a rigid surface. For the different temperatures of the sample, the P0-SIVR distribution presents a wide maximum, whose intensity decreases as T increases[39], effect that is only partially due to the Debye-Waller screening of Eq. (22). On the contrary, the SIVR spectrum does not depend on T, displaying a sharp peak at the specular reflection angle $\theta_f = \theta_i$, i.e., on the Laue circle.

The θ_f profile for a given Bragg maximum was estimated to follow a lognormal behavior as a consequence of the effect of thermal vibrations[131,167,168]. Then, a standard procedure is to fit the broad polar distribution using a lognormal function[12,40]:

$$\mathscr{P}(\theta_f) = \frac{A}{\omega\ \theta_f} \exp[\frac{-(ln(\theta_f/\theta_c))^2}{2\omega^2}], \qquad (23)$$

where A, θ_c, and ω are fitting parameters. This fitting was applied to the P0-SIVR results of Fig. 17 (green dot-dashed line), finding that Eq. (23) describes quite well the simulations, with a lognormal width ω slightly increasing with T[39].

Concerning the polar width of the GIFAD patterns, in Ref.[131], by assuming a pure repulsive mean surface potential defined as $V_0 \exp(-\Gamma Z)$, with Z the atom-surface distance, the lognormal width of Eq. (23) was estimated as $\omega = \Gamma \langle u_z^2 \rangle^{1/2}$, with $\langle u_z^2 \rangle$ being the mean-square vibrational amplitude normal to the surface plane. But this behavior is not followed by the ω values obtained from the P0-SIVR approach (see Fig. 6 of Ref.[39], noting that the lognormal width differs by a factor 2 from that given by Eq. (23)), from which it is possible to roughly estimate a parameter Γ that is much smaller than the *stiffness* of the potential, defined as the normalized slope of the mean surface potential $(-[V(Z)]^{-1} dV/dZ)$ evaluated in the region of the projectile reflection[40]. This discrepancy might be associated with the influence of soft potential effects[17,55,133], not taken into account in Ref.[131], as well as with the neglect of the attractive forces, which was found to provide an excessively simplified description of the surface potential in the framework of GIFAD[40]. Furthermore, since the P0-SIVR approach for zero-phonon scattering does not include inelastic processes associated with net phonon excitations, it is reasonable that the polar dispersion of the experimental GIFAD patterns exceeds the one predicted by the P0-SIVR approach[38,39].

From the experimental point of view, the separation of the elastic contribution from the inelastic phonon-mediated one in GIFAD spectra represents a difficult task[12,37,40,154]. Schram and Heller[166] proposed an additional interference method to distinguish elastic from inelastic GIFAD, which is still awaiting experimental confirmation. But in Refs.[12,37,40] this was done by fitting the experimental polar-angle profile with a combination of a narrow Gaussian function and a wide lognormal distribution [Eq. (23)], which represent the elastic and inelastic contributions respectively. As an example, Fig. 18 shows the experimentally-derived lognormal width ω, as a function of the normal energy, for Ne atoms grazingly impinging along the [110] channel of LiF(001) at room temperature, under different incidence conditions[40]. These data show that the polar width of the inelastic contribution decreases when $E_\perp$ increases until $E_\perp \sim 100$ meV, and then it reaches a plateau. A similar behavior was also observed for

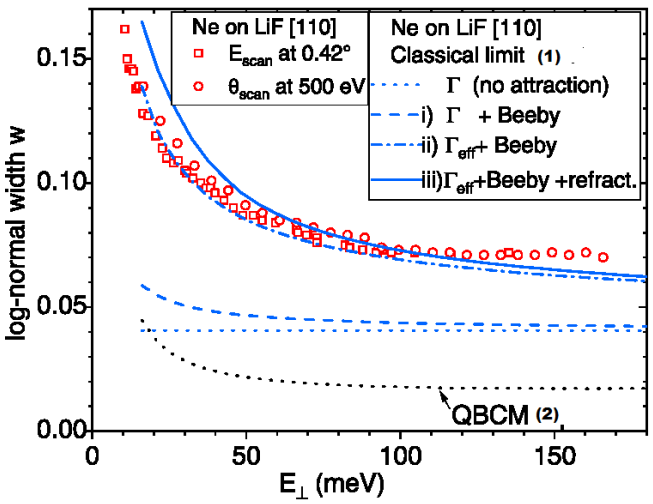

Fig. 18 (Color online) Lognormal width ω of the inelastic polar-angle profile (corresponding to Eq. (23)) as a function of the normal energy $E_\perp$, for Ne atoms impinging on a LiF(001) surface under the conditions indicated in the left inset. Symbols, experimentally-derived data[40]. Lines, QBCM results and incomplete QBMC approaches, as explained in the right inset, considering (1) the classical limit and (2) the binomial statistic of inelastic events along the projectile path, as respectively given by Eqs. 5 (b) and 5 (a) of Ref.[40]. Reprinted with permission from (P. Pan, M. Debiossac and P. Roncin, Phys. Rev. B, Polar inelastic profiles in fast-atom diffraction at surfaces, **104**, 165415 (2021)). Copyright (2021) by the American Physical Society.

He projectiles. Moreover, in this latter case, the experimentally-derived ω values were found to be independent of the incidence channel.

In order to account for the inelastic phonon-mediated scattering, Ref.[37] by Roncin and Co. presents a quantum binary collision model (QBCM) based on classical projectile trajectories scattered off an ideal rigid surface. Within the QBCM, the projectile dynamics is split up in a succession of smooth binary collisions, where the elastic (p_e) or inelastic ($1-p_e$) probabilities for each binary collision are evaluated from a local Debye oscillator model, being expressed in terms of the classical recoil energy. But first results within this QBCM[37,165] were obtained by using a purely repulsive surface potential, which was recently found to be an overly restrictive and simplified approach[40].

With regard to the contribution of attractive forces, they play a key role in GIFAD from insulating surfaces, specially at low normal energies[15,17,55]. Consequently, the QBCM was recently extended[40] to include an attractive term in the mean surface potential, which is expressed as an analytic Morse potential with a potential well of depth D. To take into account the effects associated with the presence of this attractive well, the QBCM was modified by incorporating the Beeby correction in the incoming path (i.e., a positive shift $+D$ of the effective normal energy), an effective stiffness $\Gamma_{eff}(Z) = -[E_\perp + D]^{-1}\, dV/dZ$ of the surface potential at the projectile turning point, and the refraction of the inelastically-scattered projectiles in the outgoing path (i.e., a negative shift of the median final polar angle ($\overline{\theta}_f$) given by $\left[\overline{\theta}_f^2 - D/E\right]^{1/2}$). Results derived within this improved QBCM, together with partial results containing each of these corrections, are also shown in Fig. 18 by assuming the classical limit, i.e., that all the binary collisions are inelastic. From this figure, it is observed that the classical limit of the QBCM is in very good agreement with the experimentally-derived ω values, but the model underestimates the experiment when the standard binomial statistics for inelastic binary collisions along the projectile trajectory is used[40]. Moreover, this QBCM is not able to quantitatively predict the ratio of elastic diffraction and the angular shift of the maximum of the inelastic distribution, features whose proper description requires a more deeply study, as discussed in Ref.[40].

Lastly, despite the extremely good cleanness of crystal surfaces used in GIFAD experiments, other source of incoherent contributions might be related to the presence of surface defects, like ad-atoms or steps[40]. These factors deserve further research both theoretically and experimentally in the next future[45]. Therefore, the proper description of inelastic GIFAD currently represents a challenge for the theory.

3.2.5 Incoherente electronic excitations

As it had been early foreseen for insulating targets, the electronic excitations were experimentally found to contribute slightly to the quantum decoherence of He/LiF(001) GIFAD[162]. However, when helium projectiles are replaced with the more reactive hydrogen atoms, excitonic and ejected-electron excitations become a relevant mechanism of decoherence, which introduces a diffuse background in the projectile distributions, along with a measurable projectile energy loss[13,162]. Moreover, GIFAD patterns in conjunction with meaningful energy losses were experimentally detected for metal surfaces, like silver[24].

In the case of metals, electron excitations are considered to yield the most important contribution against quantum coherence. First experimental studies on these inelastic effects were carried out for the He/Ag(110) system[24]. Latter on, in Ref.[164] the electron-excitation contribution for this collision system was estimated within a semiclassical approach by using electron-He elastic cross sections taken from gas phase experiments, combined with a surface electron density derived from a simple jellium model.

The inelastic contribution due to electronic excitations in the crystal can be assumed as completely incoherent[154] because such electronic transitions allow one to trace back the projectile pathways[169]. Thence, in Ref.[163] this contribution was evaluated by means of a semiclassical formalism that takes into account the energy lost by the projectile along the classical trajectory, but without including effects of quantum coherence. Within this inelastic scattering model, the classical projectile paths are obtained by including a friction force in the corresponding Newton's equations. The friction force is expressed in terms of the transport cross section, at the Fermi level, for the atomic projectile embedded in a surface electron gas[170], whose electron density is evaluated from the same 3D DFT calculation than the PES. In Fig. 19 the experimental energy-loss distribution for 0.5 keV ^{3}He atoms scattered off Ag(110) along the $[1\bar{1}2]$ channel[164,171] is fairly well described by the simulations, which include the experimental energy spread of the incident beam through a convolution[163]. In addition, Fig.

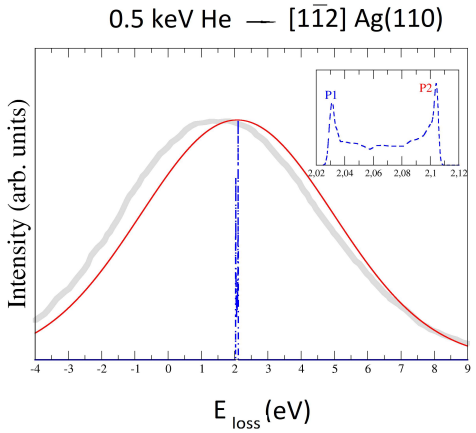

Fig. 19 (Color online) Energy-loss spectrum, as a function of the lost energy E_{loss}, for ^{3}He atoms scattered off Ag(110) surface along the $[1\bar{1}2]$ direction. The incidence energy and angle are $E = 0.5$ keV and $\theta_i = 1.5^o$, respectively. Blue dashed line, differential energy-loss probability for a mono-energetic incident beam (primary spectrum); red solid line, differential probability convoluted to include the experimental energy spread; gray solid line, experimental data from Ref.[164,171]. Inset: Detail of the primary spectrum. Reprinted with permission from (C. A. Ríos-Rubiano, M. S. Gravielle, J. I. Juaristi, Phys. Rev. A, Energy-loss contribution to grazing scattering of fast He atoms from a silver surface, **89**, 032706, 2014). Copyright (2014) by the American Physical Society.

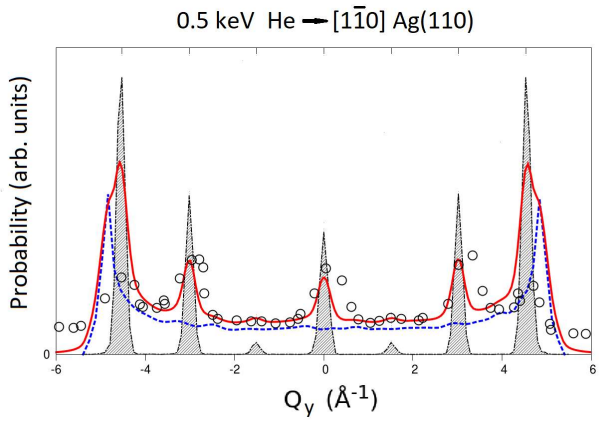

Fig. 20 (Color online) Momentum distribution, as a function of the transverse momentum transfer $Q_y = K_f \cos\theta_f \sin\varphi_f$, for ^{3}He atoms impinging on Ag(110) along the $[1\bar{1}0]$ direction. The incidence energy and angle are $E = 0.5$ keV and $\theta_i = 0.75^o$, respectively. Solid red line, total differential momentum probability obtained by adding elastic and inelastic contributions, as explained in the text; dashed blue line, inelastic contribution due to electron excitations; black dashed line (shading curve), elastic contribution evaluated within the SE approach[82]; empty circles, experimental data from Ref.[24]. Reprinted with permission from (C. A. Ríos-Rubiano, M. S. Gravielle, J. I. Juaristi, Phys. Rev. A, Energy-loss contribution to grazing scattering of fast He atoms from a silver surface, **89**, 032706, 2014). Copyright (2014) by the American Physical Society.

19 also displays the primary spectrum (blue dashed line) derived by considering an ideal mono-energetic incident beam, which presents maxima at the lowest and highest lost-energy values (labeled as P1 and P2 in the inset). These peaks are associated with projectiles that move in the middle and over the rows forming the channel, respectively. But the observation of such energy-loss structures, which might provide detailed information about the trajectory-dependent energy loss, requires an energy resolution that is beyond of current experiments, so the peaks become completely washed out when the experimental initial conditions are considered.

The inelastic-scattering model described above can be also used to evaluate the corresponding projectile distribution, which needs to be added to the elastic one to account for the experimental patterns[163]. For example, for ^{3}He incidence on Ag(110) along the $[1\bar{1}0]$ direction, in Fig. 20 we show the projectile distribution obtained by adding the elastic (SE approach[82]) and the inelastic spectra, where the relative weight of inelastic scattering was estimated as 75% to adjust the experiment[163]. From this figure, we observe that the inelastic probability corresponding to different electron-hole pair excitations (considered as incoherent processes) presents an almost flat behavior, with only two maxima at the outermost transverse transferred momenta Q_y, which are related to rainbow scattering. Whereas the elastic spectrum displays well defined Bragg peaks, that combined with the inelastic distribution, reproduce very well the experimental pattern, except for the rainbow maxima that are overestimated as a consequence of the classical rainbow divergence[134].

Finally, it should be noticed that the study of the electron-excitation contribution has been mainly confined to He/Ag(110) GIFAD. Thus, a systematic and deeper study of this topic would be desirable.

3.3 Quantum simulations

GIFAD can be simulated using a time-dependent wave-packet propagation (TDWP) method[172,173], a quantum treatment that has been widely used for TEAS and TEMS[89,174,175]. As described in detail in Refs.[176], in applying this method one has to solve the 3D time-dependent Schrödinger equation:

$$i\frac{\partial}{\partial t}\Psi(\mathbf{r},t) = \hat{H}\Psi(\mathbf{r},t), \tag{24}$$

with $\mathbf{r} = (x,y,z)$. By using the reference system shown in Fig. 1 ((x,y) plane parallel to the surface), the wave function $\Psi(\mathbf{r},\mathbf{t})$ can be written as:

$$\Psi(\mathbf{r},t)) = e^{ik_x x + ik_y y - i(k_x^2+k_y^2)t/2m_p}\,\psi(\mathbf{r},t), \tag{25}$$

$\psi(\mathbf{r},\mathbf{t})$ being a periodic function in x and y coordinates. Thus, the terms of the Hamiltonian operator, $\hat{H} = \hat{T}(\mathbf{r}) + \hat{V}_T(\mathbf{r})$, are given by:

$$\hat{T}(\mathbf{r}) = -\frac{1}{2m_p}\left(\frac{\partial}{\partial x} + ik_x\right)^2 - \frac{1}{2m_p}\left(\frac{\partial}{\partial y} + ik_y\right)^2 - \frac{k_x^2+k_y^2}{2m_p} - \frac{1}{2m_p}\frac{\partial^2}{\partial z^2} \tag{26}$$

and

$$\hat{V}_T(\mathbf{r}) = \hat{V}(\mathbf{r}) + \hat{V}_{Abs}(\mathbf{r}), \tag{27}$$

where $\hat{V}(\mathbf{r})$ represents the projectile-surface PES and $\hat{V}_{Abs}(\mathbf{r})$ a complex absorbing potential.

The initial wave function, $\psi(\mathbf{r},\mathbf{0})$, is described by a Gaussian wave packet along the z direction, such as

$$\psi(\mathbf{r},0) = e^{-ik_z z} e^{-(z-z_0)/\gamma^2}, \tag{28}$$

where γ is the width of the wave packet. The wave packet is usually propagated using the split-operator method [177] and at the end of the propagation, the wave function is absorbed by a complex absorbing potential to reduce the total propagation time avoiding discontinuities in the wave function. The scattered wave functions can be analyzed using the virtual-detector method [178], and the diffraction probabilities can be calculated as the ratio between the flux in a given diffracted direction and the incidence flux through the plane parallel to the surface (see Ref. [176] for further details).

However, for GIFAD one can work with the axial surface channeling approximation (ASCA) that reduces substantially the computational time. In applying this approximation the effect of the surface potential corrugation along the incidence beam direction is neglected, because diffraction occurs perpendicular to the incidence direction. In this case, for an incidence direction along x, the 3D time-dependent Schrödinger equation is replaced by:

$$i\frac{\partial}{\partial t}\Psi(y,z,t) = \hat{H}\Psi(y,z,t). \tag{29}$$

$\hat{V}(x,y,z)$ is replaced by $\hat{V}(y,z)$ and $\hat{T}$ is rewritten as:

$$\hat{T} = -\frac{1}{2m_p}\left(\frac{\partial}{\partial y} + ik_y\right)^2 - \frac{k_y^2}{2m_p} - \frac{1}{2m_p}\frac{\partial^2}{\partial z^2} \tag{30}$$

The ASCA has shown to yield excellent results, in comparison with fully dimensional quantum methods, when GIFAD conditions are fully met [176,179]. In fact, the agreement between 3D and 2D simulations can be seem as a fingerprint of GIFAD as long as $\lambda_\perp$ is similar to the surface periodicity parameter across the channel. So that incidence conditions for which an excellent agreement is met are GIFAD conditions. In Fig. 2 of Ref. [176] it is shown an example of the comparison between the 3D results and those obtained within the ASCA framework for ^{3}He reflection from LiF(001) along the [110] crystallographic direction. From this figure, we can see that the agreement worsens when the incidence energy parallel to the surface decreases and/or the incidence angles increases, because in this case the condition $a_x << E\ [\tan\theta_i(\partial V/\partial z)]^{-1}$, which ensures that the molecule feels a periodic potential along the incidence direction, is not completely fulfilled. Although, in principle, the ASCA should be only valid for incidence along a low-index crystallographic direction, it has been also shown [179] that this approximation still holds for an angular misalignment as large as $\pm\ 12^\circ$.

The ASCA has been widely used to simulate GIFAD, not only for the benchmark system He/LiF(001) [2,14,176,179–181], for which it has been found, for example, that the atomic beam can be trapped on the surface, traveling macroscopic distances (up to 0.2 μm) preserving its coherence. But also for Ne/LiF(001) [15], where from the comparison between simulated and experimental Bragg-peak intensities for several diffraction orders, it was possible to obtain an accurate empirical description of the attractive potential well. And even more complex systems, such a graphene adsorbed on 6H-SiC(0001) [182], where the good agreement between theory and experiments has allowed to extract detailed information about the corrugation of the system, revealing the ability of GIFAD to identify Moiré structures of graphene adsorbed on surfaces. It proves that this technique could play an important role in determining Moiré structures of graphene in metal substrates, a timely topic where contradictory experimental results called for more accurate surface sensitive experimental techniques [183,184]. This method has been also used to study the $\beta_2(2\times4)$ reconstructured GaAs(001) surface [20,21]. It is also worth mentioning that ASCA-TDWP, in combination with an atom-surface potential that includes the effect of thermal lattice vibrations by averaging the PES over the vibrational fluctuations of each surface ion, has been used to extract an accurate surface rumpling for He/LiF(001) [146].

However, the ASCA may fail in reproducing GIFAD, for example, for surfaces with a large lattice parameter, such as reconstructed surfaces or periodic superstructures adsorbed on a surface, because as mentioned above, the condition $a_x << E\ [\tan\theta_i(\partial V/\partial z)]^{-1}$ is not entirely achieved. A detailed analysis of this phenomenon has been performed using model potentials whose only difference is the lattice parameter value [180]. From Fig. 2 of Ref. [180], where diffraction probabilities computed at 3D TDWP theory level for these model potentials are shown, it can be observed that specular diffraction probabilities remain constant for lattice parameter values from 5.37 a.u., the one corresponding to LiF(001), up to 26.8 a.u. Furthermore, for values higher than 26.8 a.u. non-negligible diffraction probabilities are found along the incidence direction, proving that ASCA cannot be used for lattice parameters larger than 26.8 a.u. Of course, the specific lattice parameter value from which ASCA fails will depend on the specific characteristic of the surface. For example, diffraction peaks along crystallographic directions different from the perpendicular to the incidence one, e.i., different from the typical diffraction peaks found in GIFAD, has been observed in GIFAD measurements for H diffraction from the reconstructed surface $Al_2O_3(11\bar{2}0)$, where the lattice parameter values are 62.36 and 116.03 a.u. along the crystallographic directions $[\bar{1}100]$ and $[\bar{1}101]$, respectively.

A different approach to perform 3D quantum simulations, reducing the computational cost of the TDWP method, is the multi configuration time-dependent Hartree (MCTDH) [185–187]. Within the MCTDH framework, the 3D wave function, $\Psi(\mathbf{r},t)$, is written as a sum of products of single-particle functions (SFPs):

$$\Psi(\mathbf{r},t) = \sum_{j_1=1}^{n_1} \cdots \sum_{j_f=1}^{n_f} D_{j_1,\ldots,j_f}(t) \prod_{k=1}^{f} \varphi_{j_k}^{(k)}(q_k,t), \tag{31}$$

where f denote the number of degrees of freedom (DOFs), $D_{j_1,\ldots,j_f}$ denote the time-dependent expansion coefficients, $\varphi_{j_k}^{(k)}(q_k,t)$ the time-dependent SPFs, k denote the k^{th} nuclear coordinate, and n_k the number of SPFs used to describe each DOF. The SPFs are expanded in a time-independent primitive bases func-

tions as:

$$\varphi_{j_k}^{(k)}(q_k,t) = \sum_{i_k=1}^{N_k} d_{i_k,j_k}^{(k)}(t)\chi_{i_k}^{(k)}(q_k). \quad (32)$$

Within this formalism the equations of motions for both the expansion coefficients and the SPFs are derived from the Dirac-Frenkel variational principle, $\langle \delta\Psi|H - i(\partial/\partial t)|\Psi\rangle = 0$, leading to a set of coupled equations that request less computational effort to be solved than the TDWP method. This is so because the wave function is expanded in a much smaller number of SPFs than the number of time-independent basis functions typically required in the TDWP method. Note that, as in the case of the TWDP method, a complex absorbing potential is placed in the non-interaction region to absorb the reflected wave function avoiding discontinuities, and the diffraction probabilities are obtained from the flux analysis of the reflected wave function.

At this point, it is worth mentioning that the MCTDH method is extremely more efficient when combined with a PES that has also the form of a sum of products of one-dimensional functions [186]. To transform any non-separable 3D PES into a product of 1D functions, one can use the POTFIT algorithm [188,189], which allows one to write the 3D-PES as:

$$V(\mathbf{r},t) \approx V^{app} = \sum_{j_1=1}^{m_1} \cdots \sum_{j_f=1}^{m_f} C_{j_1,\ldots,j_f} u_{j_1}(q_1)\ldots u_{j_f}(q_f), \quad (33)$$

f being equal to 3, and the expansion coefficients, C_j, are calculated as the overlaps between the potential $V(\mathbf{r},t)$ and the so-called natural potential u_j, so that

$$C_{j_1,\ldots,j_f} = \sum_{i_1=1}^{m_1} \cdots \sum_{i_f=1}^{m_f} V_{i_1,\ldots,i_f} u_{i_1 j_1}\ldots u_{i_f j_f}. \quad (34)$$

These natural potentials are the orthogonal eigenvectors of the symmetric positive semidefinite potential energy density matrices $\rho^{(k)}$, given by:

$$\rho_{jl}^{(k)} = \sum_{i_1=1}^{N_1} \cdots \sum_{i_{k-1}=1}^{N_{k-1}} \sum_{i_{k+1}=1}^{N_{k+1}} \cdots \sum_{i_f=1}^{N_f} V_{i_1\ldots i_{k-1} j i_{k+1}\ldots i_f} V_{i_1\ldots i_{k-1} l i_{k+1}\ldots i_f}. \quad (35)$$

Eventually, to improve the potential fits in the regions relevant for the dynamics, a modified reference potential V' is defined as:

$$V'_{i_1,\ldots,i_p} = w_{i_1,\ldots,i_p} V_{i_1,\ldots,i_p} + (1 - w_{i_1,\ldots,i_p}) V^{app}_{i_1,\ldots,i_p}. \quad (36)$$

Here w is chosen so that w=1 in the region relevant for the dynamics, and w<1 in the rest of the configurations space. Within this procedure one can reduce the computational resources required. To avoid numerical inaccuracies in the potential fitting procedure of the repulsive regions, a maximum potential value can be set in the POTFIT iteration procedure.

MCTDH simulations have been used to study, for example, H GIFAD from LiF(001) [115], where it was found that simulations reproduce nicely the experimental trend observed for diffraction probabilities as a function of the normal incidence energy (see Fig. 21 (a)). The use of MCTDH also allows to perform systematic studies, as the one performed for H/LiF(001) as a function of the incidence angle [115]. This systematic study revealed that GIFAD conditions are already reached for incidence angles as high as 5° and for total incidence energies as lower as 40 eV. This work also showed that for low normal incidence energies, GIFAD results can be mimicked by performing simulations at normal incidence at the same normal energy and looking only at the diffraction peaks allowed in GIFAD for the desired incidence direction. MCTDH has also been used to perform GIFAD simulations for H/KCl(001) and He/KCl(001) [85] which, as discussed in Sec. 2.3, have allowed to assess the role of vdW dispersion forces on these systems.

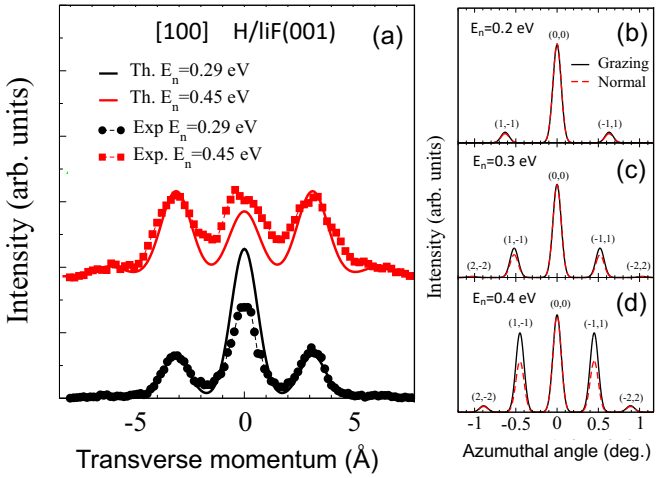

Fig. 21 Color online Diffraction spectra for H/LiF(000) along the crystallographic direction [100]. (a) Comparison between 3D-MCTDH (θ_i = 5°) and experimental results. (b)-(d) Comparison between MCTDH simulated diffraction spectra at grazing incidence and at normal energy for several normal incidence energies. In the case of normal incidence, only diffraction peaks present at grazing are considered. The theoretical results have been convoluted with a 1D Gaussian function to simulate the experimental spread. Reprinted from Nucl. Instrum. Meth. Phys. Res. B **382**, 49-53, 2016, A. S. Muzas, F. Gatti, F. Martín, C. Díaz, Diffraction of H from LiF(001): From slow normal incidence to fast grazing incidence, copyright (2016) with permission from Elsevier.

GIFAD diffraction patterns can be also simulated using an open quantum system approach [155,190], in which the Liouville-van Neumann equation for the density operator of the entangled system atomic wave packet and surface is reduced to a Lindbland equation, which in turn is solved using a quantum trajectory Monte Carlo (QTMC) method [191]. This method has been used to extract the buckling surface parameter for LiF(001) from He/LiF(001) experimental GIFAD patterns [155]. Despite this success, the used of QTMC to simulate GIFAD has not become very widespread.

Finally, it should be mentioned that recently the Close Coupling method, widely used to describe TEAS [192], has been successfully used to described Ne GIFAD from LiF(001) [15].

4 Grazing incidence fast molecules diffraction (GIFMD)

In comparison with GIFAD, GIFMD has received much less attention, and only few theoretical and experimental studies are available in the literature. However, as in the case of TEMS, light molecules, such as H_2 and D_2, are easier to generate than H, and in the case of H_2, this molecule is lighter that He, which may re-

duce the effect of surface-phonon inelastic processes risen from the molecule-surface collision. Furthermore, thanks to the internal DOFs, molecular projectiles allow for a deeper exploration of the surface characteristics, including its reactivity properties, as we will show in Sec. 4.1.

4.1 Classical approximation

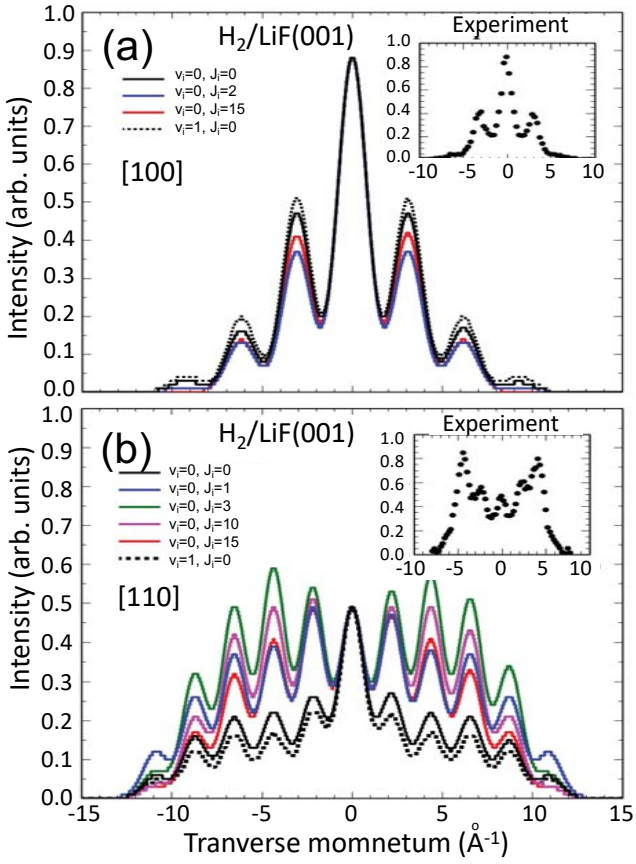

Fig. 22 (Color online) Diffractograms for H_2/LiF(001) simulated using a classical binning method, for several rovibrational states, along the crystallographic directions [100] (a) and [110] (b). The normal energy used is 300 meV. The insets show the experimental diffractograms. Adapted from Ref.[193] under Creative Commons Attribution 3.0 License

Although to obtain accurate GIFMD results quantum calculations are required, the classical binning method discussed in Sec. 3.1 can also be used to obtain qualitative results for GIFMD at a very low computational cost. For example, binning results for H_2/LiF(001)[193] reproduce fairly well the experimental diffractogram along the [100] direction (see Fig 22 (a)), a direction where results does not seem to depend on the initial rovibrational state. For incidence along the [110] direction (Fig 22 (b)), on the other hand, the shape of the diffractogram (the relative diffraction-peak probability) depends strongly on the initial rotational state, but still binning results reproduce qualitative the experimental one if one considers only initial rotational values $J > 0$. These binning results suggested that most of the molecules in the experimental beam are rotationally excited, which was later confirmed by quantum simulations[194] (see Fig. 24).

The reasonable good results obtained for GIFMD using the binning method should not be that surprising if one notices that the same method was previously used successfully to study diffraction at quasi-normal and quasi-thermal energies[195,196], and the binning is better the smaller the parallel momentum change that defines the Wigner-Seitz cell. Thus, the higher the incidence energy the smaller the Wigner-Seitz cell, and therefore, the closer the binning to the quantized values, and the better the results obtained. At this point, it is worthy to remark that the binning method is only useful in systems where phonons and electron-hole pairs excitations play a negligible role.

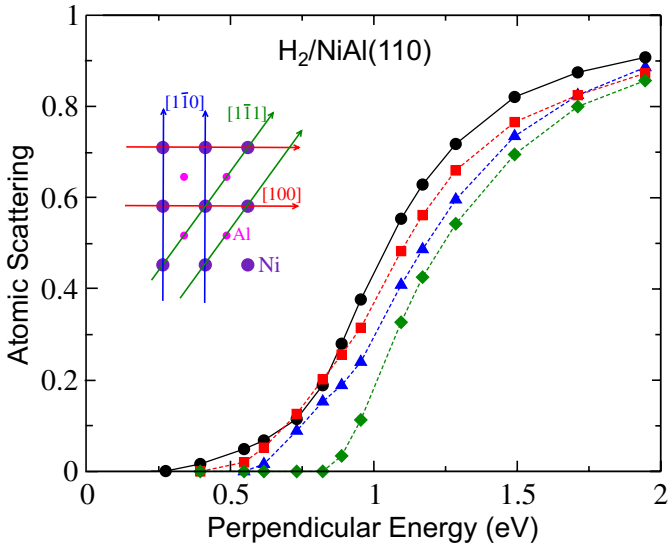

Fig. 23 (Color onlin) Atomic reflectivity for H_2(v=0,J=0)/NiAl(110) under GIFMD incidence conditions as a function of the perpendicular incidence energy. Red squares, blue triangles and green diamonds represent results along the crystallographic directions [100], [1$\bar{1}$0] and [1$\bar{1}$1], respectively. Black circles the dissociative adsorption probability obtained at low normal incidence energy. The inset shows the crystallographic direction as well as the channel width defined as the distance between nearest parallel rows of equivalent atoms along a given direction. Adapted with permission from[197]. Copyrighted by the American Physical Society 1997.

Beyond diffraction simulations, classical dynamics can be also used to study reactive scattering under fast grazing incidence conditions[197–199]. These scattering simulations have shown that it is possible to determine sticking probabilities at thermal and quasi-thermal energies, from the threshold up to the saturation limit, by analysing molecular scattering under fast grazing incidence. Under these extreme conditions a molecule behaves much as it does under normal incidence and low incidence energy, i.e., it can be reflected or dissociated. Although, contrary to reactive TEMS, under GIFAD conditions the dissociated atoms do not get adsorbed on the surface, due to their parallel energy, but are scattered. Thus, by looking at the scattered atoms as a function of their perpendicular energy, one can mimic the dissociative adsorption curve at low energy and normal incidence from the threshold up to the saturation limit. In Fig. 23, we show an example of such a

phenomenon for the activated* system H_2/NiAl(110). From this figure, one can see that the agreement between GIFMD dynamics, which proceeds in a channeling regime [200], and low normal incidence results is better the wider the GIFMD scattering channel, because the narrower the channel the greater the probability that the molecule hit the potential barrier and scatter before breaking. Nevertheless, the agreement is reasonable along any incidence direction, and more important, all GIFMD curves tend to the same saturation value, the one found theoretically at low incidence energy. This study showed that GIFMD experiments could become an ideal complement to traditional molecular beam experiments at low energy, where the saturation limit is hard to reach [201]. This behavior of the atomic reflectivity as a function of the perpendicular energy, mimicking the dissociative adsorption curve obtained at low energy and normal incidence, has also been found for non-activated† systems [197,198]. Furthermore, GIFMD simulations have also been able to reproduce the transition from monotonous to non-monotonous dissociative adsorption probabilities found for activated systems upon the increasing of the initial vibrational state [199].

4.2 Quantum simulations

To perform 6D (see Fig. 4 (a)) simulations one has to solve also Eq. (24), but now the Hamiltonian operator is more complex, due to the internal DOFs. In this case, the Hamiltonian representing the systems is given by:

$$\hat{H} = -\frac{1}{2m_p}\frac{\partial^2}{\partial z^2} - \frac{1}{2m_p sin^2\gamma_m}\left[\frac{\partial^2}{\partial x^2} - 2cos\gamma_m \frac{\partial}{\partial x}\frac{\partial}{\partial y} + \frac{\partial^2}{\partial y^2}\right] - \frac{1}{2\mu}\frac{\partial^2}{\partial r^2} + \frac{\hat{J}^2}{2\mu r^2} + V(x,y,x,r,\theta_m,\varphi_m), \quad (37)$$

where m_p and μ are the mass and the reduced mass of the molecules, respectively, γ_m is the skewing angle, i.e., the angle between the lattice vectors $\mathbf{a}_x$ and $\mathbf{a}_y$, which takes the value 90° for square and rectangular lattices and 60° for hexagonal lattices, and $\hat{J}$ represents the rotational operator, whose eigenfunctions are the spherical harmonics $Y_J^{M_J}(\theta_m,\varphi_m)$.

To solve Eq.(24) we can use either the TDWP or the MCTDH methods discussed in Sec. 3.3, although, in this case, we have three extra DOFs corresponding to the internal motion of the molecule (r, θ_m, φ_m). In applying the TDWP method [89], the dependence of the wave function on X_{cm}, Y_{cm}, Z_{cm}, and r is represented by a direct product discrete variable representation (DVR), and on θ_m and φ_m by a nondirect product finite basis representation (FBR) of spherical harmonics. Gauss-associated-Legendre and Fourier transforms are used to transform the wave function from FBR to DVR, and vice versa [203]. The initial wave function in this case is written as:

$$\Phi_0^{6D}(\mathbf{R},0) = \upsilon_{v,J}(r)Y_J^{M_J}(\theta,\varphi)\frac{1}{\sqrt{A}}e^{i\mathbf{K}_0\mathbf{R}_\parallel}\int dk_{Z_{cm}} b(k_{Z_{cm}})\frac{1}{\sqrt{2\pi}}e^{ik_{Z_{cm}}Z_{cm}}, \quad (38)$$

i.e., as a product of the vibrational and rotational eigenfunctions, a plane wave function, describing the parallel translation motion,

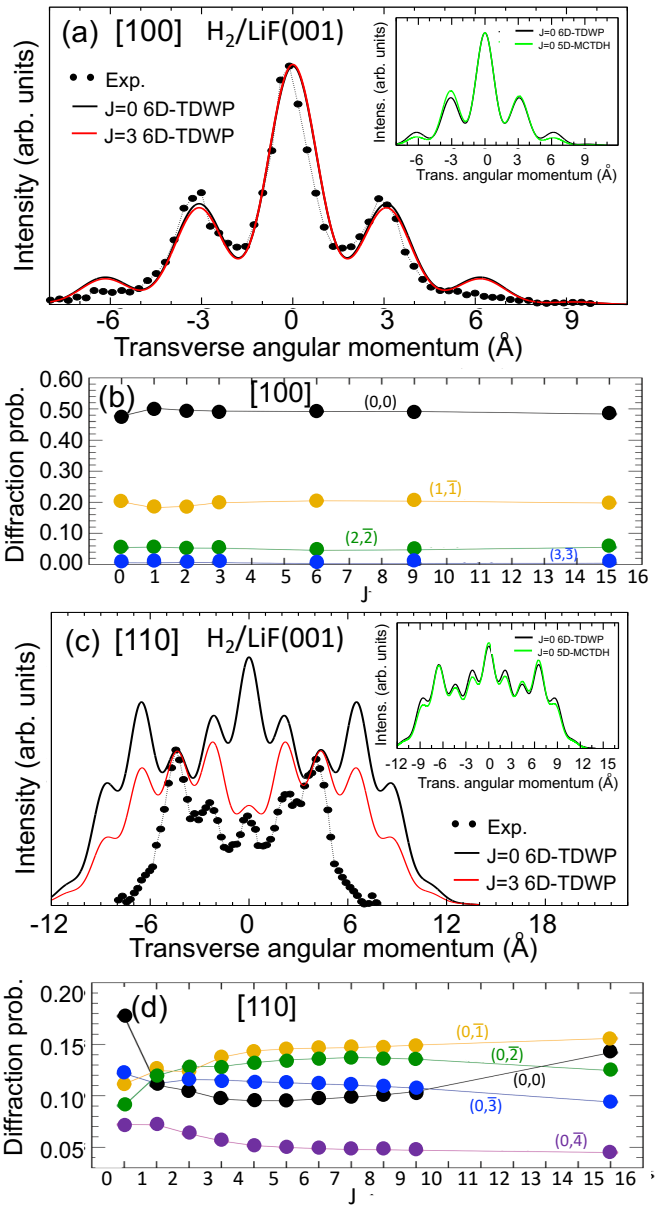

Fig. 24 (Color online). Theoretical and experimental diffractograms obtained for H_2 GIFMD from LiF(001) along the crystallographic directions [100] (a) and [110] (c). The insets show the comparison between 6D-TDWP and 5D-MCTHD simulated diffractograms. Panels reprinted with permission from (A. S. Muzas, M. del Cueto, F. Gatti, M. F. Somers, G. J. Kroes, F. Martín, C. Díaz, Phys. Rev. B, H_2/LiF(001) diffractive scattering under fast grazing incidence using a DFT-based potential energy surface, **96**, 205432, 2017). Copyright (2017) by the American Physical Society. (b) and (d) panels show the probability of diffraction peaks as a function of the initial rotational state along the [100] and [110] crystallographic directions, respectively. Panels reproduced from [194] with permission from the Royal Society of Chemistry, copyright 2017.

* A system presenting a minimum reaction barrier, for which the dissociative adsorption probability increases monotonously with the energy [87].

† A system that does not present a minimum reaction barrier, for which the dissociative adsorption probability shows a non-monotonously behavior as a function of the energy [87].

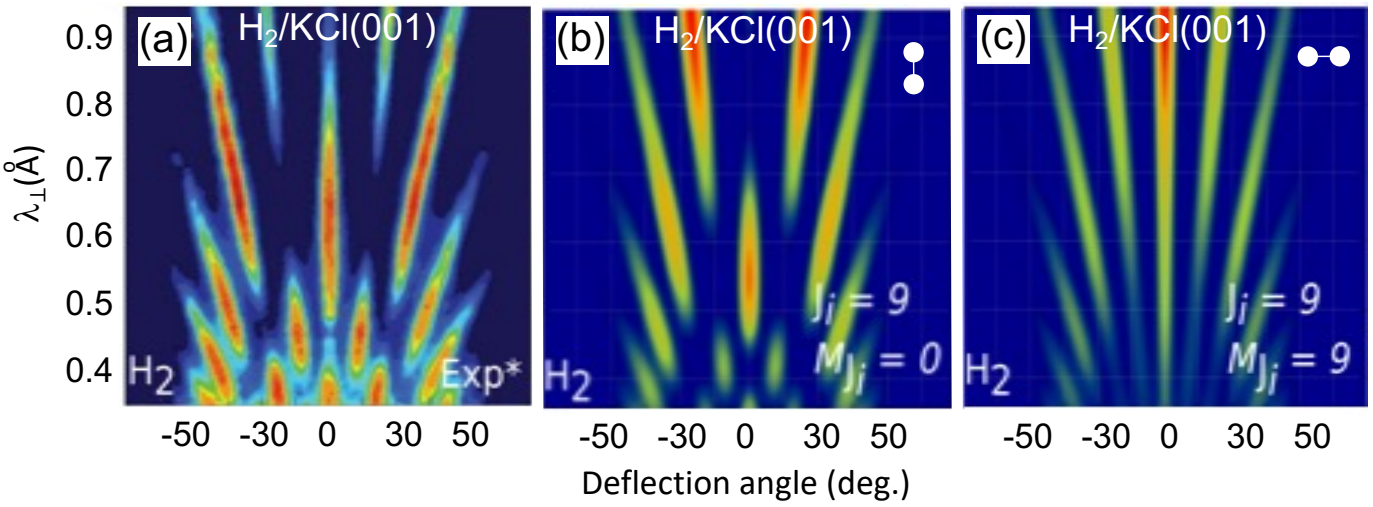

Fig. 25 (Color online) GIFMD pattern along the incidence crystallographic direction [100] for H_2/KCl(001). (a) Experimental results taken from Ref.[202]; (b) Helicopter orientation; (c) Cartwheel orientation.

and a Gaussian wave packet, describing the perpendicular translation motion. In this expression $\mathbf{R}_{\parallel} = (X_{cm}, Y_{cm})$, $\mathbf{K}_0$ represents the initial parallel momentum and A the unit cell area used to build the 6D-PES. As in the 3D case, the wave function is propagated using the split operator method[177]. The backscattering wave function is gradually absorbed by a complex absorbing potential, and it is analyzed using the Balint-Kurti formalism[204–206].

In applying the MCTHD method, one has to use Eqs. (31) to (35), with $f = 6$ (6 DOFs). But, to further reduce the computational time the modes (X_{cm},Y_{cm}), (Z_{cm},r), and (θ_m,φ_m) are combined in the SPFs, so that

$$\Psi(\mathbf{R},\mathbf{t}) = \sum_{h=1}^{N_{X_{cm}Y_{cm}}} \sum_{k=1}^{N_{Z_{cm}r}} \sum_{l=1}^{N_{\theta_m\varphi_m}} A_{hkl}(t)\varphi_h(X_{cm}Y_{cm};t)\varphi_k(Z_{cm}r;t)\varphi_l(\theta_m\varphi_m;t). \quad (39)$$

Both TDWP and MCTDH methods have been used to study H_2/LiF(001)[86,194]. In Fig. 24 (a) and (c), we show the diffractograms obtained from 6D-TDWP and 5D-MCTDH simulations. In this later case, the vibrational DOF is not taken into account. From the comparison between these two types of simulations (see insets Fig. 24 (a) and (c)), it was concluded that the vibrational DOF plays a negligible role in H_2 GIFMD from LiF(001), and by extension in similar systems. On the contrary, for H_2/metal surface the vibration mode could not be neglected because, as discussed in Sec. 4.1, the molecule can break up during the scattering process. From the comparison between 6D-TDWP simulations and experimental results, it was concluded, as anticipated by the classical binning method (see Fig. 22), that diffraction is independent of the initial rotational state (J) for diffraction along the [100] crystallographic direction (see Fig. 24 (b)), whereas it is strongly dependent on the J value along the [110] direction. Along the [100] direction, theoretical diffractograms are in excellent agreement with the experimental one[119], as shown in Fig. 24 (a), independently of the initial rotational state. As deduced from Fig. 24 (b), this conclusion hold, at least, for J values up to J=15 (the maximum J value evaluated). On the other hand, along the [110] direction the agreement is rather poor (see Fig. 24 (c)), worse for J=0 than for J=3. In fact, as shown in Fig. 24 (d) the probability of the different diffraction peaks depend strongly on the J value, the (0,0) peak being the one that depends the most on J (see Fig. 24 (c)).

As shown in Ref.[194], the different behavior found for H_2 GIFMD from LiF(001) along the [100] and [110] channels can be explained in terms of the electrostatic quadrupole-ionic lattice interaction. This conclusion was supported by a thorough analysis based on the analytical PES developed by Hill[207,208], which has been found to yield similar diffraction results as the DFT-based PES[86]. As already pointed out in Sec. 2.1, analytical potentials allow one to study individually the different physical mechanisms that contribute to the whole PES. In the case of H_2-LiF(001), we distinguish five contributions, namely, the repulsive and an attractive pair potentials, the induce dipole-dipole quadrupole interaction, the ionic lattice-induced dipole interaction, and the electrostatic quadrupole-ionic lattice interaction (V_{els}). This latter term is proportional to $\sum_{n,m} D_{nm}(\theta_m,\varphi_m)[1-(-1)^{n+m}]$. For incidence along the [100] direction, $n+m$ is always even (see Fig. 8), thus the contribution of V_{els} is always zero and only low diffraction peaks could be expected. For incidence along the [110] diffraction, on the other hand, $n+m$ is even and odd alternatively, leading to a non-negligible role of V_{els}, and therefore, to the presence of higher diffraction-order peaks in the diffractograms. Furthermore, the term V_{els} explains the different shape found for $J = 0$ and $J > 0$ diffractograms. As $D_{nm}(\theta_m,\varphi_m)$ only involves second order spherical harmonics, $\langle Y_0^0|V_{els}|Y_0^0\rangle = 0$ for J=0, which reflects the fact that for $J = 0$ all molecular orientations are equally likely. On the other hand, molecules with $J > 0$ have a net orientation, and therefore, they are affected by V_{els}.

It is also important to mention that for the two molecular systems theoretically studied so far, H_2/LiF(001)[86,194] and H_2/KCl(001), the vast majority of diffracted molecules retain their initial J value. This result has relevant consequences for the further development of experimental techniques. As rotation-

ally inelastic diffraction can be safety neglected when interpreting molecular diffractograms, it does not see crucial to develop techniques that discriminate between scattered molecules with different J values, as far as insulating crystals are considered.

Very interesting results, that claim from further GIFMD experiments, have been found very recently for H_2/KCl(001) [209]. Quantum GIFMD simulations have shown a strong stereodinamics effect. Molecules impinging perpendicular (cartwheel orientation, i.e., $M_J = 0$), or quasi-perpendicular, to the surface display diffraction spectra in good agreement with the experimental ones, whereas those molecules impinging parallel (helicopter orientation, i.e., $M_J = J$), or tilted, to the surface show diffraction spectra rather different from the experimental ones. In Fig. 25, we show an example of this phenomenon for incidence along the [100] crystallographic direction, and the molecule in the rovibrational state ($v = 0$, $J = 9$). Based on a theoretical analysis,

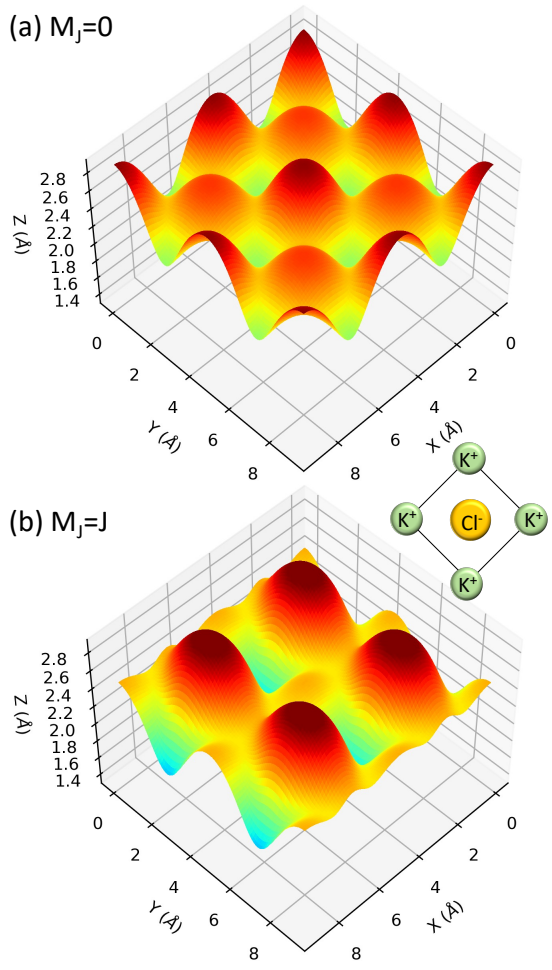

Fig. 26 (Color online) 3D representations of the H_2/KCl(001) classical turning points (Z(Å)) for a perpendicular energy equal to 64 meV (similar results are found for higher energies). (a) Cartwheel orientation; (b) Helicopter orientation. The inset shows the KCl(001) unit cell. Orange balls represent Cl^- and green balls K^+.

this stereodynamics effect can be understood from the combination of the corrugation felt by the molecules according to their orientation and the supernumerary rainbow theory (SRT) [11]. A simple analysis of the PES over the classical turning point reveals that cartwheel molecules feel a similar, but not equal, corrugation over the K^+ and the Cl^- sites, thus they see a double periodicity (see Fig. 26 (a)), which leads to two types of diffracted trajectories. According the SRT, the interference between these two wave-paths produced by the double periodicity leads to diffraction patterns where some peaks vanish (as shown in Fig. 25 (b)). Same conclusion can be reached using form factor arguments. On the other hand, helicopter molecules only feel the corrugation due to Cl^-, since the corrugation due to K^+ is much smaller. Thus, they see a single periodicity (see Fig. 26 (b)), which leads to only one type of diffracted trajectories and to diffraction patterns with all diffraction peaks present (see Fig. 26 (c)). Understanding the origin of this stereodynamics effect in the experiment is more puzzling and would require more experimental measurements to be unraveled.

5 Outlook and final remarks

GIFAD has been a widely used technique during the last 15 years, which rationalizes the theoretical effort invested aiming to simulate, analyze and extract accurate information from the experimental measurements. As a results of this intense work, dynamics simulations have improved every year, from the developing of more accurate atom-surface potential models and the inclusion of vdW dispersion forces to the description of phenomena that may influence the experimental measurements, such as projectile coherence and inelastic scattering processes. Specially relevant has been the inclusion of phonons through a semiclassical dynamics approach, which allows one to account for thermal effects in GIFAD, as well as the recent efforts to understand the effect of inelastic phonon contributions.

Over this time, much work has been devoted to the full quantum description of GIFAD, developing and adapting methods that certainly offer a rigorous representation of atomic scattering from a given surface potential. Among these methods, we find the time-dependent wave packet propagation, the multiconfiguration time-dependent Hartree, the quantum trajectory Monte Carlo, and close coupling methods. All these methods allow one to consider the full dimensionality of the problem within the surface static approximation, and in an approximate manner, the surface thermal fluctuations (phonons). However, from these quantum methods it is difficult to disentangle the contribution of the different physical mechanisms involved in GIFAD, and in this regard, the semiclassical (or semiquantum) approximations represent a very useful tool. Semiclassical methods were not only key to understand the unexpected first GIFAD measurements but were also often used to extract information about the morphological and electronic characteristics of surfaces from experimental patterns.

In relation to the use of GIFAD as a surface analysis technique, it is worth mentioning that its extraordinary sensitivity has positioned it as one of the most accurate instruments to test PESs at normal energies ranging from ten to a few thousand meV. Precisely this remarkable feature was recently used to derive precise empirical atom-surface potentials from the contrast of experimental Bragg intensities with full quantum calculations [15]. But from the theoretical point of view, such correctness requirements for

the description of the surface potential represent both a challenge and an opportunity for the improvement of ab initio theoretical models, including the developing of appropriate vdW functionals.

Furthermore, it should be noticed that although much effort has been put into the correct representation of elastic scattering from ideal crystal surfaces, which is the main mechanism of GIFAD, interference experiments are often affected by other factors or processes that disrupt coherence, this being a less studied issue. Among these factors, the coherence of the incident beam, which is determined by the collimating setup and the incidence conditions, plays an important role, affecting the overall structure of the diffraction patterns. Although it was verified experimentally that it is possible to control the interference mechanism that governs the projectile distributions by varying the size of the collimating slit[154], it would be desirable to have a systematic experimental study on this effect. This would allow not only to confirm the theoretical predictions about the influence of the degree of coherence of the incident atom, but also to understand under what conditions the classical limit (fully incoherent) is reached. Additionally, such a experimental research would be of interest for the study of other processes, like atomic collisions involving atoms and molecules as targets[210–213], for which the influence of the projectile coherence is currently under debate[214–217].

Decoherent contributions on GIFAD represent also a scarcely studied problem, which has only recently received renewed attention. In particular, the effect due to thermal lattice vibrations, which has been suspected from the beginning of destroying quantum coherence. Although there have been some early attempts to describe thermal effects, most theoretical methods are based on the use of a rigid surface model, neglecting phonon contributions. Lately, however, two different theoretical models - QBCM and P-SIVR - have been developed to deal with phonon-mediated scattering from insulating materials. While the former provides a qualitative description of elastic and inelastic probabilities by combining classical trajectories scattered from a rigid surface with a local Debye oscillator model[37], the latter is a semiquantum approach that includes a more realistic description of the surface, given by the quantum harmonic-crystal model[38]. P-SIVR results for zero-phonon scattering (i.e., without net phonon exchange) show that the thermal fluctuations of the lattice introduce a wide polar-angle dispersion into the angular distributions[39], which transform the interference spots into elongated structures, like it is experimentally observed. But this polar spread is smaller than the experimental measured, suggesting that there are other processes, like inelastic phonon excitations, that contribute to the formation of the interference streaks. In turn, an improved version of the QBCM[40], including corrections associated with the presence of a physisorption well in the potential, has shown to offer a very good representation, in the classical limit, of the broad width of experimental polar profiles. However, the description of other features of the polar distributions needs a deeper and more systematic study. Thence, the contribution of inelastic phonon-mediated scattering to GIFAD is nowadays an open problem that is calling for more experimental and theoretical work. Other effects that still remain on the list of pending research topics are the influence of surface defects, like steps, vacancies or ad-atoms, and the contribution of electron excitations in the case of metals.

GIFMD, on the other hand, has received much less attention. In spite of the fact that the presence of the internal DOFs of the molecule confers to this technique functionalities beyond those of GIFAD. On the one hand, H_2 (and D_2) projectiles could be more enlightening for the characterization of the surface properties. For example, the large anisotropic electronic interaction between the quadrupole moment of the molecule and the electric field created by the ionic crystal leads to an enhancement of the intensity of high-order diffraction peaks in some incidence crystallographic directions, rendering more detailed information about the surface characteristics. However, to fully develop this potential of GIFMD further improvements of the experimental setups are required. For example, theoretical simulations have shown a strong dependence on the initial rotational state, but contrary to TEMS state-of-the-art setups, which can distinguish and/or select the rotational state of the molecule[218–221], the current apparatus used in GIFMD experiments does not allow either to estimate the distribution of rotational states in the molecular beam or to select a initial rotational state. Furthermore, current experimental setups do not allow either to distinguish the final rotational state of the scattered molecules, although for ionic surfaces this development should be less relevant because, as shown by the theoretical simulations, rotational excitations are negligible in GIFMD from ionic surfaces.

In the case of metal surfaces, GIFMD experiments are required to test the theoretical finding according to which is possible to mimic dissociative adsorption probabilities curves at low energy and normal incidence by measuring atomic scattering upon GIFMD. As the angle between the two scattered atom trajectories is higher than 2°, this experimental measurements are, hypothetically, feasible. The achievement of such experiments would allow one to indirectly measured dissociative adsorption probabilities from the threshold to the saturation value, which is not possible nowadays with standard low-energy molecular-beam techniques, such as the popular King-Wells technique[222]. Therefore, this achievement would have a significant impact in the field of molecular dissociation on metal surfaces at low energy, and in turn, on the closely related field of catalyzed molecular reactivity processes.

The effort to invest in GIFMD should not only come from the experimental side, but also from the theory. Theoretical methods have to evolve in order to include more DOFs. Some attempts to include the surface DOFs in diatomic molecule-surface interactions, far from a properly description of phonons modes, have been carried out at low energy and normal, or quasi normal, incidence. These attempts include the simple oscillator model[223,224] and the most elaborated Langevin oscilator model[225,226] in classical dynamics, a phonon sudden approximation[227] in 6D quantum dynamics, and a 7D quantum dynamics, in which the motion of second layer surface is included in the wavefunction[227]. But none of these methods have been used yet to study GIFMD. The inclusion of electronic excitations in the dynamic is still a pending subject. Several approaches to include the effects of electron-hole pair excitations have been proposed for reactive TEMS[170,228], but how to extend this approaches to GIFMD is still a pending task for

theorists. The inclusion of both phonons and electron-hole pair excitations in GIFMD are the main challenges that theorists will have to be faced in the coming future.

In summary, despite the enormous experimental and theoretical effort invested in GIFAD and GIFMD, which has resulted in the current degree of development of this technique, there is still room for improvement to place it, in the medium term, in a leadership position for surface analysis.

List of acronyms

ASCA: Axial surface channeling approximation
CRP: Corrugation reducing procedure
CTMC: Classical trajectory Monte Carlo
DFT: Density functional theory
DOFs: Degrees of freedom
DVR: Discrete variable representation
FBR: Finite basis representation
GGA: Generalized gradient approximation
GIFAD: Grazing incidence fast atom diffraction
GIFAS: Grazing incidence fast atom scattering
GIFMD: Grazing incidence fast molecule diffraction
HCW: Hard-corrugated wall
IVR: Initial value representation
LDA: Local density approximation
MCTDH: Multi-configuration time-dependent Hartree
MSI: Modified Shepard interpolation
NN: Neural networks
PA: Pairwise additive
PAW: projector augmented wave
PBC: Periodic boundary conditions
PES: Potential energy surface
PIP-NN: permutation invariant polynomial neural networks
P-SIVR: Phonon-surface initial value representation
P*n*-SIVR: Phonon-surface initial value representation for *n*-phonon scattering
QBCM: Quantum binary collision model
QTMC: Quantum trajectory Monte Carlo
RFF: Reactive force fields
SE: Surface eikonal
SIVR: Surface initial value representation
SPF: Single particle function
SRT: Supernumerary rainbow theory
TDWP: Time-dependent wave-packet propagation
TEAS: Thermal-energy atom scattering
TEMS: Thermal-energy molecule scattering
vdW: van der Waals

List of symbols

$a^{()}$: Partial transition amplitude
$a_{x(y)}$: Periodicity lattice parameter along $x(y)$
a: Real lattice vector
$A^{()}$: Transition amplitude
$\mathscr{A}_{n_{ph}}$: Effective transition amplitude for n_{ph}-phonon scattering
b: Reciprocal lattice vector
$c_{\mathbf{r}_\mathrm{B}}$: Evjen caging factor for the lattice site $\mathbf{r}_\mathrm{B}$
χ: Time-independent primitive function
d: Atomic basis set vector
D: Depth of the attractive well of the mean surface potential
$\Delta K_x^{\parallel}$: Longitudinal momentum change parallel to surface plane
$\Delta K_y^{\parallel}$: Transverse momentum change parallel to surface plane
$\Delta K_z^{\perp}$: Momentum change perpendicular to surface plane
E: Incidence energy
$\mathrm{E}_\perp$: Perpendicular incidence energy
E_{r_B}: Electric field originated by the asymptotic ionic charge at $\mathbf{r}_\mathrm{B}$
f_s: Spatial profile of the incident wave-packet
f_m: Momentum profile of the incident wave-packet
F: Atomic form factor
G: Gaussian function
G: reciprocal lattice vector
$\hat{H}$: Hamiltonian operator
j_0: Spherical Bessel function
J: Rotational quantum number of a diatomic molecule
J_M: Maslov function
$\hat{J}$: Rotational operator
k_B: Boltzman constant
$\mathbf{k}_o$: Initial momentum vector of the classical projectile trajectory
$\mathbf{k}_t$: Time-dependent classical momentum of the projectile
$\mathbf{K}_i$: Initial projectile momentum
$\mathbf{K}_f$: Final projectile momentum
L: Distance between the surface and the collimating aperture
λ: de Broglie wavelength of the incident projectile
$\lambda_\perp$: Perpendicular de Broglie wavelength of the incident projectile
m_p: Projectile mass
μ: Projectile reduced mass
μ_{coh}: Complex degree of coherence
M_J: Magnetic rotational quantum number of a diatomic molecule
$n^{(O)}_{\mathbf{r}_\mathrm{B}}$: radial *onion* density of the crystal ion at $\mathbf{r}_\mathrm{B}$
N: Number of equivalent channels that are coherently illuminated
N_c: Number of atoms in the crystal sample
N_l: Bose-Einstein occupation function
Ω_f: Solid angle corresponding to the $\mathbf{K}_f$ direction
Ω_0: Solid angle corresponding to the $\mathbf{k}_o$ direction
$P^{()}$: Scattering probability
Ψ: Wave function
Q: Transferred momentum vector of the projectile
$\mathbf{r}_\mathrm{B}$: Bravais position vector
$\mathbf{r}_o$: Initial position vector of the classical projectile trajectory
$\mathbf{r}_t$: Time-dependent classical position of the projectile
R: Position of the molecule with respect to the surface
$s_{x(y)}$: Length of the longitudinal (transverse) side of the collimating slit
S_g: Geometrical structure factor
S_N: Intra-channel interference factor
σ: Transverse coherence length
θ_i: Angle of incidence with respect to the surface plane
θ_f: Scattering angle with respect to the surface plane
θ_m Polar angle between the molecule bond and the z-axis
Θ: Deflection angle
Θ_{rb} Rainbow deflection angle

T: Temperature of the crystal
$\hat{T}$: Kinetic energy operator
u_j: Natural potential
$\upsilon_{v,J}$: Vibrational eigenfunctions
φ: Time-dependent single particle function
φ_i: Azimuthal angle between the projection on yx of the incidence direction and the x-axis
φ_f: Azimuthal angle between the projection on yx of the scattered direction and the x-axis
φ_m: Azimuthal angle between the projection on xy of the molecule bond and the x-axis
$\mathbf{u}$: Displacement of the crystal ion with respect to its equilibrium position
$\underline{\mathbf{u}}_o$: Displacement vector of all the crystal ions of the sample, with respect to their equilibrium positions, at the starting time $t = 0$
$v_{\mathbf{r}_B}^{(\text{short})}$: Short-range interaction between the atomic projectile and a crystal ion placed at $\mathbf{r}_B$
$\langle u_z{}^2 \rangle$: Mean-square vibrational amplitude of crystal ions normal to the surface plane
v: Vibrational quantum number of a diatomic molecule
$\widetilde{v}$: Fourier transform of the binary interaction between an atom and a crystal ion
V: Periodic projectile-surface potential
$\hat{V}$: Potential energy operator
V_{Abs}: Complex absorbing potential
$W^{(\text{long})}$: Long-range atom-surface interaction
$\mathbf{W}_{\mathbf{r}_B}(\mathbf{q})$ Momentum-dependent Debye-Waller function at the lattice site $\mathbf{r}_B$
ω_I: Phonon Frequency
$Y_J^{M_J}$: Spherical harmonics
$Z_{\mathbf{r}_B}^{(asym)}$: Asymptotic charge of the crystal ion placed at $\mathbf{r}_B$
$Z_{A(O)}$: Nuclear charge of the atom (*onion*)

Conflicts of interest

There are no conflicts to declare.

Acknowledgements

The authors acknowledge financial support from MICINN (PID2019-106732GB-I00) of Spain, and from CONICET (PIP 2014-11220130100386CO) and ANPCyT (PICT- 2017-1201 and PICT-2017-2945) of Argentina. Most of the work described here has been possible thanks to the contribution of Alberto S. Muzas, Marcos del Cuento, Leandro Frisco, Carlos Ríos Rubiano, Gisela Bocan, Fernando Martín, and Jorge Miraglia.

Notes and references

1 A. Schüller, S. Wethekam and H. Winter, *Phys. Rev. Lett.*, 2007, **98**, 016103.
2 P. Rousseau, H. Klemliche, A. G. Borisov and P. Roncin, *Phys. Rev. Lett.*, 2007, **98**, 016104.
3 H. Hoinkes, *Rev. Mod. Phys.*, 1980, **52**, 933.
4 D. Frankl, *Prog. Surf. Sci.*, 1983, **13**, 285.
5 J. Barker and D. Auerbach, *Surf. Sci. Rep.*, 1984, **4**, 1.
6 D. Farías and K.-H. Rieder, *Rep. Prog. Phys.*, 1998, **61**, 1575–1664, and references therein.
7 D. Farías and R. Miranda, *Prog. Surf. Sci.*, 2011, **86**, 222.
8 D. Farías, C. Díaz, P. Nieto, A. Salin and F. Martín, *Chem. Phys. Lett.*, 2004, **390**, 250.
9 A. Schüller, H. Winter, M. S. Gravielle, J. M. Pruneda and J. E. Miraglia, *Phys. Rev. A*, 2009, **80**, 062903.
10 A. Schüller and H. Winter, *Nucl. Instrum. Meth. Phys. Res. B*, 2009, **267**, 628–633.
11 H. Winter and A. Schüller, *Prog. Surf. Sci.*, 2011, **86**, 169–221.
12 M. Debiossac, P. Pan and P. Roncin, *Phys. Chem. Chem. Phys.*, 2021, **23**, 7615–7636.
13 J. Lienemann, A. Schüller, D. Blauth, J. Seifert, S. Wethekam, M. Busch, K. Maass and H. Winter, *Phys. Rev. Lett.*, 2011, **106**, 067602.
14 M. Debiossac, A. Zugarramurdi, P. Lunca-Popa, A. Momeni, H. Khemliche, A. G. Borisov and P. Roncin, *Phys. Rev. Lett.*, 2014, **112**, 023203.
15 M. Debiossac, P. Roncin and A. G. Borisov, *J. Phys. Chem. Lett.*, 2020, **11**, 4564–4569.
16 B. Lalmi, H. Khemliche, A. Momeni, P. Soulisse and P. Roncin, *J. Phys.: Condens Matter*, 2012, **24**, 442002.
17 G. A. Bocan, H. Breiss, S. Szilasi, A. Momeni, E. M. Staicu-Casagrande, M. S. Gravielle, E. A. Sánchez and H. Khemliche, *Phys. Rev. Lett.*, 2020, **125**, 096101.
18 M. Busch, E. Meyer, K. Irmscher, Z. Galazka, K. Gärtner and H. Winter, *Appl. Phys. Lett.*, 2014, **105**, 051603.
19 H. Khemliche, P. Rousseau, P. Roncin, V. H. Etgens and F. Finocchi, *Appl. Phys. Lett.*, 2009, **95**, 151901.
20 M. Debiossac, A. Zugarramurdi, H. Khemliche, P. Roncin, A. G. Borisov, A. Momeni, P. Atkinson, M. Eddrief, F. Finocchi and V. H. Etgens, *Phys. Rev. B*, 2014, **90**, 155308.
21 M. Debiossac, P. Atkinson, A. Zugarramurdi, M. Eddrief, F. Finacchi, V. H. Etgens, A. Momeni, H. Khemliche, A. G. Borisov and P. Roncin, *Appl. Surf. sci*, 2017, **391**, 53.
22 M. Busch, J. Seifert, E. Meyer and H. Winter, *Phys. Rev. B*, 2012, **86**, 241402.
23 J. Seifert, E. Meyer and H. Winter, *Nucl. Instrum. Meth. Phys. Res. B*, 2013, **317**, 90.
24 N. Bundaleski, H. Khemliche, P. Soulisse and P. Roncin, *Phys. Rev. Lett.*, 2008, **101**, 177601.
25 M. Busch, A. Schüller, S. Wethekam and H. Winter, *Surf. Sci*, 2009, **603**, L23.
26 A. Schüller, M. Busch, J. Seifert, S. Wethekam, H. Winter and K. Gärtner, *Phys. Rev. B*, 2009, **79**, 235425.
27 A. Schüller, M. Busch, S. Wethekam and H. Winter, *Phys. Rev. Lett.*, 2009, **102**, 017602.
28 J. Seifert and H. Winter, *Phys. Rev. Lett.*, 2012, **108**, 065503.
29 M. Debiossac, A. Zugarramurdi, Z. Mu, P. Lunca-Popa, A. J. Mayne and P. Roncin, *Phys. Rev. B*, 2016, **94**, 205403.
30 J. Seifert and H. Winter, *Surf. Sci.*, 2009, **L109**, 603.
31 J. Seifert, A. Schüller, H. Winter, R. Wlodarczyk, J. Sauer and M. Sierka, *Phys. Rev. B*, 2010, **82**, 035436.

32 J. Seifert, M. Busch, E. Meyer and H. Winter, *Phys. Rev. Lett.*, 2013, **111**, 137601.

33 J. Seifert, M. Busch, E. Meyer and H. Winter, *Phys. Rev. B*, 2014, **89**, 075404.

34 P. Atkinson, M. Eddrief, V. H. Etgens, H. Khemliche, M. Debiossac, A. Momeni, M. Mulier, B. Lalmi and P. Roncin, *Appl. Phys. Lett.*, 2014, **105**, 021602.

35 A. Momeni, E. M. Staicu-Casagrande, A. Dechaux and H. Khemliche, *J. Phys. Chem. Lett.*, 2018, **9**, 908.

36 M. S. Gravielle, J. E. Miraglia and G. A. Bocan, in *State-of-the-Art Reviews on Energetic Ion-Atom and Ion-Molecule Collisions, Interdisciplinary Research on Particle Collisions and Quantitative Spectroscopy*, World Scientific, Singapore, 2019, vol. 2, ch. 7, p. 177–203.

37 P. Roncin and M. Debiossac, *Phys. Rev. B*, 2017, **96**, 035415.

38 L. Frisco and M. S. Gravielle, *Phys. Rev. A*, 2019, **100**, 062703.

39 L. Frisco and M. S. Gravielle, *Phys. Rev. A*, 2020, **102**, 062821.

40 P. Pan, M. Debiossac and P. Roncin, *Phys. Rev. B*, 2021, **104**, 165415.

41 J. E. Miraglia and M. S. Gravielle, *Phys. Rev. A*, 2017, **95**, 022710.

42 M. S. Gravielle and J. E. Miraglia, *Nucl. Instrum. Meth. Phys. Res. B*, 2009, **267**, 610–614.

43 M. S. Gravielle, A. Schüller, H. Winter and J. E. Miraglia, *Nucl. Instrum. Meth. Phys. Res. B*, 2011, **269**, 1208–1211.

44 M. S. Gravielle and J. E. Miraglia, *Phys. Rev. A*, 2014, **90**, 052718.

45 L. Frisco and M. S. Gravielle, *to be published*.

46 V. Celli, D. Eichenauer, A. Kaufhold and J. P. Toennies, *J. Chem. Phys.*, 1985, **83**, 2504–2521.

47 P. W. Fowler and J. M. Hutson, *Phys. Rev. B*, 1986, **33**, 3724–3751.

48 D. Eichenauer and J. P. Toennies, *Surf. Sci.*, 1988, **197**, 267–276.

49 M. S. Gravielle, J. E. Miraglia, A. Schüller and H. Winter, *Nucl. Instrum. Meth. Phys. Res. B*, 2013, **317**, 77–82.

50 N. W. Ashcroft and N. D. Mermin, in *Solid State Physics*, Brooks/Cole, Cengage Learning, Belmont, USA, 1976.

51 J. E. Miraglia and M. S. Gravielle, *Phys. Rev. A*, 2011, **84**, 062901.

52 H. Lee, C. Lee and R. G. Parr, *Phys. Rev. A*, 1991, **44**, 768–771.

53 A. D. Becke, *Phys. Rev. A*, 1988, **38**, 3098–3100.

54 C. Lee, W. Yang and R. G. Parr, *Phys. Rev. B*, 1988, **37**, 785–789.

55 G. A. Bocan, H. Breiss, S. Szilasi, A. Momeni, E. M. Staicu-Casagrande, E. A. Sánchez, M. S. Gravielle and H. Khemliche, *Phys. Rev. B*, 2021, **104**, 235401.

56 P. Tiwald, A. Schüller, H. Winter, K. Tokesi, F. Aigner, S. Grafe, C. Lemell and J. Burgdorfer, *Phys. Rev. B*, 2010, **82**, 125453.

57 https://diamond.kist.re.kr/CSC/code/dacapo.

58 https://www.quantum-espresso.org/.

59 https://www.vasp.at/.

60 https://www.scm.com/product/adf/.

61 https://www.crystal.unito.it/index.php.

62 https://departments.icmab.es/leem/siesta/.

63 H. J. Monkhorst and J. D. Pack, *Phys. Rev. B*, 1976, **13**, 5188–5192.

64 D. J. Chadi and M. L. Cohen, *Phys. Rev. B*, 1973, **8**, 5747–5753.

65 D. R. Hamann, M. Schlüter and C. Chiang, *Phys. Rev. Lett.*, 1979, **43**, 1494–1497.

66 D. Vanderbilt, *Phys. Rev. A*, 1990, **41**, 7892.

67 P. E. Blöchl, *Phys. Rev. B*, 1994, **50**, 17953.

68 S. Ghosh, P. Verma, C. J. Cramer, L. Gagliardi and D. G. Truhlar, *Chem. Rev.*, 2018, **118**, 7249–7292.

69 P. Verna, and D. G. Truhlar, *Trends Chem.*, 2020, **2**, 302.

70 D. M. Ceperley and B. J. Alder, *Phys. Rev. Lett.*, 1980, **45**, 566–569.

71 J. P. Perdew and K. Burke, *Int. J. Quantum Chem.*, 1996, **57**, 309–319.

72 J. P. Perdew, K. BurKe and M. Ernzerhof, *Phys. Rev. Lett.*, 1996, **77**, 3865.

73 N. Mardirossian and M. Head-Gordon, *J. Chem. Theor. Comput.*, 2016, **12**, 4303–4325.

74 X. J. Shen, Y. Xiao, W. Dong, X. H. Yan and H. F. Busnengo, *Comput. Theor. Chem.*, 2012, **990**, 152.

75 S. Lorenz, A. Gross and M. Scheffler, *Chem. Phys. Lett.*, 2004, **395**, 210.

76 K. Shakouri, J. Behler, J. Meyer and G.-J. Kroes, *J. Phys. Chem. Lett.*, 2017, **8**, 2131–2136.

77 B. Jiang and H. Guo, *J. Chem. Phys.*, 2014, **141**, 034109.

78 C. Crespos, M. A. Collins, E. Pijper and G. J. Kroes, *Chem. Phys. Lett.*, 2003, **376**, 539.

79 T. J. Frankcombe, C. M. Collins and D. H. Zhang, *J. Chem. Phys.*, 2012, **137**, 144701.

80 H. F. Busnengo, A. Salin and W. Dong, *J. Chem. Phys.*, 2000, **112**, 7641.

81 M. S. Gravielle, G. A. Bocan and R. Díez-Muiño, *Phys. Rev. A*, 2010, **82**, 052904.

82 C. A. Ríos-Rubiano, G. A. Bocan, M. S. Gravielle, N. Bundaleski, H. Khemliche and P. Rocin, *Phys. Rev. A*, 2013, **87**, 012903.

83 A. S. Muzas, F. Martín and C. Díaz, *Nucl. Instr. Meth. Phys. Res. B*, 2015, **354**, 9–15.

84 G. A. Bocan, J. D. Fuhr and M. S. Gravielle, *Phys. Rev. A*, 2016, **94**, 022711.

85 M. del Cueto, A. S. Muzas, F. Martín and C. Díaz, *Nucl. Instrum. Meth. Phys. Res. B*, 2020, **476**, 1–9.

86 A. S. Muzas, M. del Cueto, F. Gatti, M. F. Somers, J. K. G, F. Martín and C. Díaz, *Phys. Rev. B*, 2017, **96**, 205432.

87 G. J. Kroes and C. Díaz, *Chem. Soc. Rev.*, 2016, **45**, 3658.

88 C. Díaz, E. Pijper, R. A. Olsen, H. F. Busnengo, D. J. Auerbach and G. J. Kroes, *Science*, 2009, **326**, 832.

89 G. J. Kroes, *Prog. Surf. Sci.*, 1999, **60**, 1.

90 G.-J. Kroes, *Phys. Chem. Chem. Phys.*, 2012, **14**, 14966–14981.

91 G. J. Kroes, *Phys. Chem. Chem. Phys*, 2021, **23**, 8962.

92 S. Grimme, *J. Comput. Chem.*, 2006, **27**, 1787–1799.

93 S. Grimme, J. Antony, S. Ehrlich and H. Krieg, *J. Chem. Phys.*, 2010, **132**, 154104.

94 S. Grimme, S. Ehrlich and L. Goerigk, *J. Comput. Chem.*, 2011, **32**, 1456–1465.

95 S. N. Steinmann and C. Corminboeuf, *J. Chem. Theor. Comput.*, 2011, **7**, 3567–3577.

96 S. N. Steinmann and C. Corminboeuf, *J. Chem. Phys.*, 2011, **134**, 044117.

97 T. Bučko, S. Lebègue, J. G. Ángyán and J. Hafner, *J. Chem. Phys.*, 2014, **141**, 034114.

98 A. Tkatchenko and M. Scheffler, *Phys. Rev. Lett.*, 2009, **102**, 073005.

99 A. Tkatchenko, R. A. DiStasio, R. Car and M. Scheffler, *Phys. Rev. Lett.*, 2012, **108**, 236402.

100 V. G. Ruiz, W. Liu, E. Zojer, M. Scheffler and A. Tkatchenko, *Phys. Rev. Lett.*, 2012, **108**, 146103.

101 M. Dion, H. Rydberg, E. Schröder, D. C. Langreth and B. I. Lundqvist, *Phys. Rev. Lett.*, 2004, **92**, 246401.

102 K. Lee, E. D. Murray, L. Kong, B. I. Lundqvist and D. C. Langreth, *Phys. Rev. B*, 2010, **82**, 081101.

103 J. C. V. Klimes, D. R. Bowler and A. Michaelides, *Phys. Rev. B*, 2011, **83**, 195131.

104 I. Hamada, *Phys. Rev. B*, 2014, **89**, 121103.

105 H. Peng, Z.-H. Yang, J. P. Perdew and J. Sun, *Phys. Rev. X*, 2016, **6**, 041005.

106 G. Román-Pérez and J. M. Soler, *Phys. Rev. Lett.*, 2009, **103**, 096102.

107 O. A. Vydrov and T. Van Voorhis, *Phys. Rev. Lett.*, 2009, **103**, 063004.

108 D. C. Langreth and B. I. Lundqvist, *Phys. Rev. Lett.*, 2010, **104**, 099303.

109 O. A. Vydrov and T. Van Voorhis, *Phys. Rev. Lett.*, 2010, **104**, 099304.

110 E. Meyer, PhD thesis, Humboldt-Universitat zu Berlin (2016).

111 M. del Cueto, A. S. Muzas, G. Füchsel, F. Gatti, F. Martín and C. Díaz, *Phys. Rev. B*, 2016, **93**, 060301.

112 R. Sabatini, T. Gorni and S. de Gironcoli, *Phys. Rev. B*, 2013, **87**, 041108.

113 G. A. Bocan and M. S. Gravielle, *Nucl. Instrum. Meth. Phys. Res. B*, 2018, **421**, 1–6.

114 M. S. Gravielle and J. E. Miraglia, *Phys. Rev. A*, 2008, **78**, 022901.

115 A. S. Muzas, F. Gatti, F. Martín and C. Díaz, *Nucl. Instr. Meth. B*, 2016, **382**, 49–53.

116 S. Wethekam and H. Winter, *Nuc. Inst. Meth. Phys. Res. B*, 2007, **258**, 48–51.

117 C. J. Ray and J. M. Bowman, *J. Chem. Phys.*, 1975, **63**, 5231–5234.

118 C. J. Ray and J. M. Bowman, *J. Chem. Phys.*, 1977, **66**, 1122–1126.

119 P. Rousseau, H. Klemliche, N. Bundaleski, P. Soulisse, A. Momeni and P. Roncin, *J. Phys.: Conf. Ser.*, 2008, **133**, 012013.

120 L. Bonnet and J.-C. Rayez, *Chem. Phys. Lett.*, 2004, **397**, 106–109.

121 A. Rodríguez-Fernández, L. Bonnet, C. Crespos, P. Larrégaray and R. Díez Muiño, *Phys. Chem. Chem. Phys.*, 2020, **22**, 22805–22814.

122 R. I. Masel, R. P. Merrill and W. H. Miller, *J. Chem. Phys.*, 1976, **64**, 45–56.

123 G. Drolshagen and E. J. Heller, *J. Chem. Phys.*, 1983, **79**, 2072–2082.

124 W. F. Avrin and R. P. Merrill, *Surf. Sci.*, 1994, **311**, 269–280.

125 J. R. Manson and K.-H. Rieder, *Phys. Rev. B*, 2000, **62**, 13142 – 13146.

126 R. Guantes, A. S. Sanz, J. Margalef-Roig and S. Miret-Artés, *Surf. Sci. Rep.*, 2004, **53**, 199–330, and references therein.

127 J. M. Moix and E. Pollak, *Phys. Rev. A*, 2009, **79**, 062507.

128 E. Pollak and S. Miret-Artés, *J. Phys.Chem. c*, 2015, **119**, 14532–14541.

129 E. A. Andreev, *Russ. J. Phys. Chem.*, 2002, **76**, S164–S169.

130 A. Schüller and H. Winter, *Phys. Rev. Lett.*, 2008, **100**, 097602.

131 J. R. Manson, H. Khemliche and P. Roncin, *Phys. Rev. B*, 2008, **78**, 155408.

132 U. Garibaldi, A. C. Levi, R. Spadacini and G. E. Tommei, *Surf. Sci.*, 1975, **48**, 649–675.

133 A. Schüller, D. Blauth, J. Seifert, M. Busch, H. Winter, K. Gärtner, R. Wlodarczyk, J. Sauer and M. Sierka, *Surf. Sci.*, 2012, **606**, 161–173.

134 S. Miret-Artés and E. Pollak, *Surf. Sci. Rep.*, 2012, **67**, 161–200, and references therein.

135 H. Winter, J. Seifert, D. Blauth, M. Busch, A. Schüler and S. Wethecam, *Appl. Surf. Sci.*, 2009, **256**, 365–370.

136 W. H. Miller, *J. Phys. Chem A*, 2001, **105**, 2942–2955, and references therein.

137 W. H. Miller, *J. Chem. Phys.*, 1970, **53**, 3578–3587.

138 X. Sun and W. H. Miller, *J. Chem. Phys.*, 1997, **106**, 916.

139 X. Sun and W. H. Miller, *J. Chem. Phys.*, 1997, **106**, 6346.

140 X. Sun and W. H. Miller, *J. Chem. Phys.*, 1998, **108**, 8870.

141 D. E. Skinner and W. H. Miller, *Chem. Phys. Lett.*, 1999, **300**, 20.

142 C. H. Dasso, M. I. Gallardo and M. Saraceno, *Phys. Rev. C*, 2007, **75**, 054611.

143 J. V. VanVleck, *Proc. Nat. Acad. Sci. USA*, 1928, **14**, 178.

144 M. S. Gravielle and J. E. Miraglia, *Phys. Rev. A*, 2015, **92**, 062709.

145 D. P. Dewangan and J. Eichler, *Phys. Rep.*, 1994, **247**, 59–219.

146 A. Schüller, S. Wethekam, D. Blauth, H. Winter, F. Aigner, N. Simonović, B. Solleder, J. Burgdörfer and L. Wirtz, *Phys. Rev. A*, 2010, **82**, 062902.

147 J.-F. Schaff, T. Langen and J. Schmiedmayer, *Riv. Nuovo Cimento*, 2014, **37**, 509–589.
148 G. Comsa, *Surf. Sci.*, 1979, **81**, 57–68.
149 A. Tonomura, in *Progress in Optics*, North-Holland, Amsterdam, 1986, vol. 23, pp. 183–220.
150 C. Keller, J. Schmiedmayer and A. Zeilinger, *Opt. Commun.*, 2000, **179**, 129.
151 C. F. Majkrzak, C. Metting, B. B. Maranville, J. A. Dura, S. Satija, T. Udovic and N. F. Berk, *Phys. Rev. A*, 2014, **89**, 033851.
152 J. M. Moix and E. Pollak, *J. Chem. Phys.*, 2011, **134**, 011103.
153 M. Minniti, C. Díaz, J. L. Fernández-Cuñado, A. Politano, D. Maccariello, F. Martín, D. Farías and R. Miranda, *J. Phys.: Condens. Matter*, 2012, **24**, 354002.
154 J. Seifert, J. Lienemann, A. Schüller and H. Winter, *Nucl. Instrum. Methods Phys. Res. B*, 2015, **350**, 99–105.
155 F. Aigner, N. Somonović, B. Solleder, L. Wirtz and J. Burgdörfer, *Phys. Rev. Lett.*, 2008, **101**, 253201.
156 M. Born and E. Wolf, in *Principles of Optics*, Pergamon Press, Oxford, 1986, ch. 10.
157 M. S. Gravielle and J. E. Miraglia, *Nucl. Instrum. Meth. Phys. Res. B*, 2016, **382**, 42–48.
158 The longitudinal coherence length may be important to resolve long periodicity intervals of the crystal surface along the incidence direction[22].
159 C. Cohen-Tannoudji, B. Diu and F. Laloë, in *Quantum Mechanics*, Willey-VCH, Paris, 2011.
160 M. S. Gravielle, J. E. Miraglia and L. Frisco, *Atoms*, 2018, **6**, 64.
161 L. Frisco, J. E. Miraglia and M. S. Gravielle, *J. Phys.: Condens. Matter*, 2018, **30**, 405001.
162 M. Busch, J. Lienemann, J. Seifert, A. Schüller and H. Winter, *Vacuum*, 2012, **86**, 1618–1623.
163 C. A. Ríos-Rubiano, G. A. Bocan, J. I. Juaristi and M. S. Gravielle, *Phys. Rev. A*, 2014, **89**, 032706.
164 N. Bundaleski, P. Soulisse, A. Momeni, H. Khemliche and P. Roncin, *Nucl. Instrum. Meth. Phys. Res. B.*, 2011, **269**, 1216–1220.
165 P. Roncin, M. Debiossac, H. Oueslati and F. Raouafi, *Nucl. Instrum. Meth. Phys. Res. B*, 2018, **427**, 100–107.
166 M. C. Schram and E. J. Heller, *Phys. Rev. A*, 2018, **98**, 022137.
167 K. Cordier, H. Khemliche and P. Roncin, LCAM-CNRS Report (unpublished), 2000.
168 J. Villete, Ph.D. thesis, Université de Paris-Sud, France, http://tel.archives-ouvertes.fr/tel-00106816/en/, 2000.
169 C. A. Ríos-Rubiano, G. A. Bocan, J. I. Juaristi and M. S. Gravielle, *Nucl. Instrum. Meth. Phys. Res. B*, 2014, **340**, 15–20.
170 J. I. Juaristi, M. Alducin, R. Díez-Muiño, H. F. Busnengo and A. Salin, *Phys. Rev. Lett.*, 2008, **100**, 116102.
171 P. Roncin (prived communication).
172 D. Kosloff and R. Kosloff, *J. Comput. Phys.*, 1988, **52**, 35.
173 A. Yinnon and R. Kosloff, *Chem. Phys. Lett.*, 1983, **102**, 216–223.
174 A. Gross, *Surf. Sci. Rep.*, 1998, **32**, 293.
175 G. J. Kroes and M. F. Somers, *J. Theor. Comput. Chem.*, 2005, **4**, 493.
176 A. Zugarramurdi and A. Borisov, *Phys. Rev. A*, 2012, **86**, 062903.
177 M. D. Feit, J. J. A. Fleck and A. Steiger, *J. Comput. Phys.*, 1982, **47**, 412.
178 J. Sjakste, A. G. Borisov, J. P. Gauyacq and A. K. Kazansky, *J. Phys. B: At. Mol. Opt. Phys.*, 2004, **37**, 1593–1603.
179 A. Zugarramurdi and A. G. Borisov, *Phys. Rev. A*, 2012, **87**, 062902.
180 A. Zugarramurdi and A. Borisov, *Nucl. Instrum. Meth. Phys. Res. B*, 2013, **317**, 83.
181 A. Zugarramurdi, M. Debiossac, P. Lunca-Popa, L. S. Alarcón, A. Momeni, H. Khemliche, P. Roncin and A. G. Borisov, *Phys. Rev. A*, 2013, **88**, 012904.
182 A. Zugarramurdi, M. Debiossac, P. Lunca-Popa, A. J. Mayne, M. A, A. G. Borisov, P. Roncin and H. Khemliche, *Appl. Phys. Lett.*, 2015, **106**, 101902.
183 J. Wintterlin and M.-L. Bocquet, *Surf. Sci.*, 2009, **603**, 1841–1852.
184 D. Stradi, S. Barja, C. Díaz, M. Garnica, B. Borca, J. J. Hinarejos, D. Sánchez-Portal, M. Alcamí, A. Arnau, A. L. Vázquez de Parga, R. Miranda and F. Martín, *Phys. Rev. Lett.*, 2011, **106**, 186102.
185 H. D. Meyer and G. A. Worth, *Theor. Chem. Acc.*, 2003, **109**, 251.
186 M. H. Beck, A. Jäckle, G. A. Worth and H. D. Meyer, *Phys. Rev.*, 2000, **324**, 1.
187 H. D. Meyer, F. Gatti and G. A. Worth, 2009.
188 A. Jäckle and H. D. Meyer, *J. Chem. Phys.*, 1996, **104**, 7974.
189 A. Jäckle and H. D. Meyer, *J. Chem. Phys.*, 1998, **109**, 3772.
190 M. Seliger, C. O. Reinhold, T. Minami, D. R. Schultz, M. S. Pindzola, S. Yoshida, J. Burgdörfer, E. Lamour, J.-P. Rozet and D. Vernhet, *Phys. Rev. A*, 2007, **75**, 032714.
191 T. Minami, C. O. Reinhold and J. Burgdörfer, *Phys. Rev. A*, 2003, **67**, 022902.
192 J. R. Manson, in *Helium atom scattering from surfaces*, Springer-Verlag, Berlin, 2013, pp. 173–205.
193 A. S. Muzas, F. Martín and C. Díaz, *J. Phys. Conf. Ser.*, 2015, **635**, 012029.
194 M. del Cueto, A. S. Muzas, M. F. Somers, G. J. Kroes, C. Díaz and F. Martín, *Phys. Chem. Chem. Phys.*, 2017, **19**, 16317.
195 D. Farías, C. Díaz, P. Rivière, H. F. Busnengo, P. Nieto, M. F. Somers, G. J. Kroes, A. Salin and F. Martín, *Phys. Rev. Lett.*, 2004, **93**, 246104.
196 C. Díaz, H. F. Busnengo, P. Rivière, D. Farías, P. Nieto, M. F. Somers, G. J. Kroes, A. Salin and F. Martín, *J. Chem. Phys.*, 2005, **122**, 154706.
197 C. Díaz, P. Rivière and F. Martín, *Phys. Rev. Lett.*, 2009, **103**, 013201.
198 C. Díaz and F. Martín, *Phys. Rev. A*, 2010, **82**, 012901.

199 D. Stradi, C. Díaz and F. Martín, *Surf. Sci.*, 2010, **604**, 2031.

200 D. S. Gemmell, *Rev. Mod. Phys.*, 1974, **46**, 129–227.

201 D. J. Auerbach, *Atomic and Molecular Beams Methods*, Oxford University Press, New York/Oxford, 1988.

202 E. Meyer, Ph. D. thesis, Humboldt-Universität zu Berlin, 2016.

203 G. C. Corey and D. Lemoine, *J. Chem. Phys.*, 1992, **97**, 4115.

204 G. G. Balint-Kurti, R. N. Dixon and C. C. Marston, *J. Chem. Soc. Faraday Trans.*, 1990, **86**, 1741.

205 G. G. Balint-Kurti, R. N. Dixon and C. C. Marston, *Int. Rev. Phys. Chem.*, 1992, **11**, 317.

206 R. C. Mowrey and G. J. Kroes, *J. Phys. Chem.*, 1995, **103**, 1216.

207 N. R. Hill, *Phys. Rev. B*, 1979, **19**, 4269.

208 G. J. Kroes and R. C. Mowrey, *J. Chem. Phys.*, 1995, **103**, 2186.

209 M. del Cueto, A. S. Muzas, F. Martín and C. Díaz, *to be published*.

210 K. N. Egodapitiya, S. Sharma, A. Hasan, A. C. Laforge, D. H. Madison, R. Moshammer and M. Schulz, *Phys. Rev. Lett.*, 2011, **106**, 153202.

211 X. Wang, K. Schneider, A. LaForge, A. Kelkar, M. Grieser, R. Moshammer, J. Ullrich, M. Schulz and D. Fischer, *J. Phys. B*, 2012, **45**, 211001.

212 H. Gassert, O. Chuluunbaatar, M. Waitz, F. Trinter, H.-K. Kim, T. Bauer, A. Laucke, C. Müller, J. Voigtsberger, M. Weller, J. Rist, M. Pitzer, S. Zeller, T. Jahnke, L. P. H. Schmidt, J. B. Williams, S. A. Zaytsev, A. A. Bulychev, K. A. Kouzakov, H. Schmidt-Böcking, R. Dörner, Y. V. Popov, and M. S. Schöffler, *Phys. Rev. Lett.*, 2016, **116**, 073201.

213 T. Arthanayaka, B. R. Lamichhane, A. Hasan, S. Gurung, J. Remolina, S. Borbély, F. Járai-Szabó, L. Nagy and M. Schulz, *J. Phys. B*, 2016, **49**, 13LT02.

214 D. V. Karlovets, G. L. Kotkin and V. G. Serbo, *Phys. Rev. A*, 2015, **92**, 052703.

215 L. Sarkadi, I. Fabre, F. Navarrete and R. O. Barrachina, *Phys. Rev. A*, 2016, **93**, 032702.

216 L. Nagy, F. Járai-Szabó and S. Borbély, *J. Phys. B*, 2018, **51**, 144005.

217 R. O. Barrachina, F. Navarrete and M. F. Ciappina, *Atoms*, 2021, **9**, 5.

218 L. C. Shackman and G. O. Sitz, *J. Chem. Phys.*, 2005, **123**, 064712.

219 E. Watts and G. O. Sitz, *J. Chem. Phys.*, 2001, **114**, 4171.

220 O. Godsi, G. Corem, Y. Alkoby, J. T. Cantin, R. V. Krems, S. M. F, J. Meyer, G. J. Kroes, T. Maniv and G. Alexandrowicz, *Nat. Commun.*, 2017, **8**, 15357.

221 Y. Alkoby, H. Chadwick, O. Godsi, H. Labiad, M. Bergin, J. T. Cantin, I. Litvin, T. Maniv and G. Alexandrowicz, *Nat. Commun.*, 2020, **11**, 3110.

222 D. A. King and M. G. Wells, *Surf. Sci.*, 1972, **29**, 454–482.

223 H. M. and H. J., *J. Phys. Chem.*, 1990, **92**, 7610.

224 H. F. Busnengo, W. Dong, P. Sautet and A. Salin, *Phys. Rev. Lett.*, 2001, **87**, 127601.

225 S. A. Adelman and J. D. Doll, *J. Chem. Phys.*, 1976, **64**, 2375.

226 J. C. Tully, G. H. Gilmer and M. Shugard, *J. Chem. Phys.*, 1979, **71**, 1630.

227 M. Bonfanti, M. F. Somers, C. Díaz, H. F. Busnengo and G. J. Kroes, *Z. Phys. Chem.*, 2013, **227**, 1397.

228 N. Shenvi, S. Roy and J. C. Tully, *Science*, 2009, **326**, 829.